Journal of Computational Electronics (2026) 25:2
https://doi.org/10.1007/s10825-025-02448-6

Wavelength-tunable equivalent circuit models for SPICE-based photonic–electronic co-simulation

Thijs Ullrick[1,2,3] · Dirk Deschrijver[1] · Domenico Spina[2] · Wim Bogaerts[3] · Tom Dhaene[1]

Received: 17 June 2025 / Accepted: 11 October 2025

Abstract
This paper introduces a SPICE-compatible photonic–electronic co-simulation framework based on the complex vector fitting (CVF) algorithm, developed for accurate representation of multi-wavelength behavior in linear and passive photonic integrated circuits (PICs). The proposed wavelength-tunable equivalent circuit models feature a fixed network topology, yet comprise components whose values are parameterized with respect to the optical carrier frequency. This enables both frequency- and time-domain simulations at arbitrary wavelengths, making the framework particularly suited for modeling multi-wavelength photonic systems. To support intricate co-simulation with electronic subsystems, a novel interface circuit is introduced, allowing seamless interconnection with third-party active and passive SPICE models. The capability of the framework to capture complex photonic–electronic interactions is demonstrated through three application examples, highlighting its effectiveness for co-simulating photonic devices with control and receiver electronics.

Keywords Circuit simulation · Complex vector fitting (CVF) · Photonic–electronic co-simulation · SPICE

1 Introduction

Driven by telecom and datacom applications and enabled by the growing maturity of today's available technology platforms, *photonic integrated circuits* (PICs) are showing a rapid growth in complexity, functionality and integration scale. Beyond traditional communication systems, the rapid rise of AI is pushing datacenters to increase data rates, leading to growing interest in PICs as hardware accelerators that enable ultra-fast, energy-efficient AI workloads. PIC-based sensors, such as on-chip spectrometers, are also emerging in environmental, biomedical, and structural monitoring. Additionally, PICs are also essential to realize (networked) quantum computers, neural networks [1–3], or LiDAR engines for cars [4].

In many of these applications, photonics needs close connections to electronics for control or read-out. Various co-integration strategies exist, but irrespective of the technological implementation, the photonics and electronics need to be designed to work together, forming a single multi-physics circuit. Traditional electromagnetic (EM) simulators are computationally too expensive for the larger geometries of these circuits. Alternatively, circuit-level abstractions leveraging hierarchy and reusable behavioral models should be used. There already exist dedicated photonic circuit design tools for schematic definition of a photonic circuit, but in practice they are used by only a minority of the photonic chip designers. So, why the hesitation? The challenges lie in the lack of standards, the low quality of the behavioral models, and the difficulty of co-simulating photonics and electronics.

✉ Thijs Ullrick
thijs.ullrick@ugent.be

Dirk Deschrijver
dirk.deschrijver@ugent.be

Domenico Spina
domenico.spina@vub.be

Wim Bogaerts
wim.bogaerts@ugent.be

Tom Dhaene
tom.dhaene@ugent.be

[1] Internet Technology and Data Science Lab (IDLab), Department of Information Technology, Ghent University - IMEC, Technologiepark-Zwijnaarde, 9052 Ghent, Belgium

[2] Department ELEC, Vrije Universiteit Brussel, Pleinlaan, 1050 Brussels, Belgium

[3] Photonics Research Group, Department of Information Technology, Ghent University - IMEC, Technologiepark-Zwijnaarde, 9052 Ghent, Belgium

Published online: 30 October 2025

Photonic signals are different from electronic signals and cannot be expressed as voltages and currents. Instead, their propagation more closely resembles that of radio-frequency (RF) signals. Photonic signals are typically represented as a modulated carrier wave that is scattered inside the connected building blocks of the photonic circuit. These bidirectional waves oscillate with a given wavelength and frequency, and at any given time can be defined by an amplitude and phase. The mismatch between photonic signals and electronic signals makes it difficult to model both together rigorously in their native formalism within the same simulation environment.

Decades of development and improvement have resulted in robust industry standards such as SPICE and Verilog-A for electronic circuit simulation. Adopting these standards for the modeling of PICs, presents a promising avenue to address the lack of standardization in photonic models, which is currently holding back the scaling to more complex circuitry. Furthermore, this approach opens up possibilities for co-simulation of both electronic and photonic circuits within a unified environment.

In general, there are two classes of PIC building blocks: (i) active or nonlinear passive devices, usually described in the time-domain, and (ii) linear passive devices whose behavior is best defined in the frequency-domain in the form of a scattering matrix. However, photonic–electronic co-simulation should always be performed in the time-domain, and this only works if there are accurate and efficient time-domain models for the linear passive devices as well. A range of models for active photonic components has been presented in the literature (e.g., lasers [5, 6], modulators [7–9], photodetectors [10–12]). However, there are only a few publications in the literature that define actual SPICE-compatible circuit models for linear passive PIC components. The contributions [13–15] demonstrate how to derive time-domain models for linear passive devices like waveguides and directional couplers; however, these models rely on simple analytic expressions derived from underlying device physics that make it very difficult to capture complex photonic phenomena such as higher-order dispersion and wavelength-dependent effects. Although computationally efficient, they often assume idealized device behavior and are only applicable to a limited range of photonic components [16, 17].

To date, only a few SPICE-based photonic–electronic co-simulation frameworks have been developed, most of which rely on the same class of simplified behavioral models. For instance, the recent EPHIC framework [18] proposes a more rigorous modeling approach by using native SPICE primitives to represent wavelength dependence and bidirectional transmission. However, its passive device models rely on simplified physical assumptions, limiting their accuracy in capturing wavelength-dependent dispersion and restricting their applicability to complex or non-standard devices (e.g., Bragg gratings, arrayed waveguide gratings). Other recent efforts have introduced Verilog-A compact models based on coupled-mode theory for four-wave mixing [19, 20]. Although the framework provides accurate results for this specific nonlinear interaction, it cannot be applied to a wide range of problems. Consequently, current frameworks lack a comprehensive and rigorous approach for modeling the complex dispersive behavior of photonic systems across broad wavelength ranges.

Recently, complex vector fitting (CVF) has been proposed to efficiently and accurately model the scattering representations of linear and passive PICs [21, 22]. Since the CVF technique builds time-domain models starting from the scattering parameters in the frequency domain, it can accurately capture complex photonic phenomena such as insertion loss, higher-order dispersion and wavelength-dependent effects. Ye et al. [23] further extended this framework by introducing the concept of equivalent voltages and currents, enabling the conversion of CVF macromodels into electrical netlists. While this advancement allows the system of ordinary differential equations (ODEs) defined by the CVF macromodel to be simulated within a SPICE environment, its applicability remains limited. The technique is restricted to linear passive circuits, does not support photonic–electronic co-simulation and necessitates the synthesis of a distinct circuit for each wavelength channel.

This paper proposes a framework for intricate photonic–electronic co-simulation across multiple wavelengths within a SPICE environment by addressing the limitations of existing equivalent circuits. Building upon the SPICE-compatible circuits of Ye et al. [21] and the wideband extension of the CVF macromodel [24], wavelength-tunable equivalent circuits with fixed topology are constructed, where component values are parameterized with respect to the optical carrier frequency, enabling simulation at arbitrary wavelengths. A real-valued baseband pole–residue representation of photonic scattering parameters is derived, enabling circuit synthesis directly from the rational approximation and thereby extending established electronic synthesis techniques to photonic systems. In addition, an interface circuit is presented to convert complex phasor representations into equivalent voltages and currents. This interface facilitates integration with third-party SPICE models and supports scalable, mixed-signal photonic–electronic co-simulation involving passive and active photonic devices, as well as control and receiver electronics.

The paper is structured as follows: Sect. 2 summarizes our prior work that forms the foundation for the more advanced parametric models and SPICE equivalent circuits. The novel contributions are outlined in Sect. 3. Section 4 discusses the derivation of the real-valued pole-residue representation and introduces a novel class of baseband pole-residue circuits. In

Sect. 5, the construction of wavelength-tunable equivalent circuits whose component values are parameterized with respect to the optical carrier frequency is presented. Section 6 leverages the wavelength-tunable circuit models to introduce a novel interface circuit and discusses key aspects of the photonic–electronic co-simulation framework. Section 7 validates the proposed modeling framework through three relevant application examples, with conclusions drawn in Sect. 8.

2 Preliminaries

For the reader's convenience, a summary of our prior work-forming the foundation for the advanced parametric SPICE circuits and the photonic–electronic co-simulation framework-is provided first.

2.1 Complex vector fitting

Complex vector fitting [21], has been presented for the frequency- and time-domain modeling of linear and passive PICs. The algorithm starts from a set of scattering parameters, acquired through measurement or simulation, defined at a discrete set of frequencies: $\mathbf{S}(f_r)$ for $r = 1, ..., R$. Next, the scattering parameters are shifted to baseband by substituting $f_i = f_r - f_c$, where f_c is the optical carrier frequency selected for system characterization. Then, once the baseband scattering parameters $\mathbf{S}_l(f_i)$ are obtained, the CVF algorithm is used to fit a rational pole-residue model

$$\mathbf{S}_l(s) = \sum_{k=0}^{K-1} \frac{\mathbf{R}_k}{s - p_k} + \mathbf{D} \tag{1}$$

where $s = j2\pi f$ is the Laplace variable, $\mathbf{R}_k \in \mathbb{C}^{n\times n}$ are the computed complex residues, p_k are the complex poles, and $\mathbf{D} \in \mathbb{R}^{n\times n}$ is a real matrix modeling the asymptotic response at high frequencies, where n is the total number of ports of the system under study. Following the derivation in [21], (1) can be analytically converted to a real-valued system of ODEs given by

$$\begin{cases} \dfrac{\mathrm{d}\hat{\mathbf{x}}(t)}{\mathrm{d}t} = \hat{\mathbf{A}}\hat{\mathbf{x}}(t) + \hat{\mathbf{B}}\hat{\mathbf{a}}(t) \\ \hat{\mathbf{b}}(t) = \hat{\mathbf{C}}\hat{\mathbf{x}}(t) + \hat{\mathbf{D}}\hat{\mathbf{a}}(t). \end{cases} \tag{2}$$

where $\hat{\mathbf{a}}(t) = [\mathbf{a}_{\Re}(t), \mathbf{a}_{\Im}(t)]$ and $\hat{\mathbf{b}}(t) = [\mathbf{b}_{\Re}(t), \mathbf{b}_{\Im}(t)]$ represent the analytic forward and backward traveling waves of the n-port baseband system, which correspond to the radio-frequency (RF) modulated envelope of the photonic signal. The state variables are denoted by $\hat{\mathbf{x}}_l(t) \in \mathbb{R}^{m\times 1}$, where $m = 2nK$. The matrix $\hat{\mathbf{A}} \in \mathbb{R}^{m\times m}$ is block-diagonal, $\hat{\mathbf{B}} \in \mathbb{R}^{m\times 2n}$ is a matrix composed of zeros and ones, $\hat{\mathbf{C}} \in \mathbb{R}^{2n\times m}$ is defined in terms of the residues $\mathbf{R}_k$, and $\hat{\mathbf{D}} \in \mathbb{R}^{2n\times 2n}$.

2.2 SPICE-compatible modeling

Most electronic circuit simulators do not directly accept differential equations as input. Therefore, the system of ODEs (2) needs to be converted into an equivalent electrical network. Given that (2) represents a system of ODEs defined at electronic frequencies [21], any of the circuit synthesis techniques that start from the state-space form can be used to convert baseband scattering parameters in an equivalent electrical network [23]. By adopting this approach, the real-valued state-space model (2) is assumed to correspond to an electronic system. Therefore, as dictated by microwave circuit theory [25], it follows that the real and imaginary photonic scattering waves of the model (2) are mapped onto electronic voltage and current signals according to (3) during the circuit synthesis step.

$$\begin{aligned} a &= \frac{V + Z_0 I}{2\sqrt{Z_0}} \\ b &= \frac{V - Z_0 I}{2\sqrt{Z_0}} \end{aligned} \tag{3}$$

In the equation above, a and b represent the forward and backward photonic scattering waves, V and I are the equivalent-circuit voltage and current variables, and Z_0 is the reference impedance defining the ratio of the voltage to current carried by the forward wave [26].

While optical waveguides also have an impedance, their scattering parameters are defined independently from it. As a result, the reference impedance in (3) can be chosen arbitrarily for modeling purposes, as long as it is real-valued [25]. The choice of the reference impedance does however affect the definition of circuit elements and needs to be carefully considered when cascading photonic circuits in a SPICE-like environment or when converting the photonic voltages and currents back to the incident and reflected waves of the scattering matrix [23]. The conversion of the real-valued CVF model, described by optical waves, to an equivalent SPICE-compatible circuit characterized by voltage and current signals is illustrated in Fig. 1.

2.3 Wideband baseband macromodels

A new state-space model, as defined by (2), must be computed using the CVF algorithm for each optical carrier frequency during time-domain characterization. In the context of wavelength-division multiplexing (WDM) systems, which may support many channels, each requiring excitation by a unique optical carrier, this method clearly exhibits poor scalability due to the substantial computational

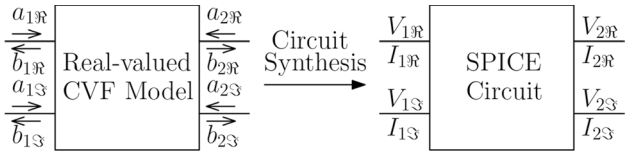

Fig. 1 Conversion of the real-valued CVF model described by (2) into an equivalent SPICE-compatible circuit. The symbols R and I indicate the real and imaginary part, respectively, of the complex port quantity (voltage or wave) considered

overhead associated with generating individual models for each carrier frequency. To address this limitation, we proposed in [24] an analytical parameterization of the CVF macromodel (1) with respect to the optical carrier frequency by strategically shifting the poles of the rational model along the imaginary axis by Δf_c in the complex plane. This parameterization yields a new system of ODEs in the form

$$\begin{cases} \dfrac{\mathrm{d}\hat{\mathbf{x}}(t)}{\mathrm{d}t} = (\hat{\mathbf{A}} - 2\pi\Delta f_c \mathbf{J}_m)\hat{\mathbf{x}}(t) + \hat{\mathbf{B}}\hat{\mathbf{a}}(t) \\ \hat{\mathbf{b}}(t) = \hat{\mathbf{C}}\hat{\mathbf{x}}(t) + \hat{\mathbf{D}}\hat{\mathbf{a}}(t). \end{cases} \tag{4}$$

where $\mathbf{J}_m = [\mathbf{0}{-}\mathbf{I};\mathbf{I}\mathbf{0}]$ with $\mathbf{0}$ and $\mathbf{I}$ representing the null and identity matrices, respectively. Expression (4) represents a new state-space model defined by the matrices $(\hat{\mathbf{A}} - 2\pi\Delta f_c \mathbf{J}_m)$, $\hat{\mathbf{B}}$, $\hat{\mathbf{C}}$ and $\hat{\mathbf{D}}$, whose center frequency $f_{cs} = f_c + \Delta f_c$ can be varied by tuning Δf_c. The key advantage of the wideband state-space model (4) as opposed to model (2) is that it can be adopted for time-domain simulations at arbitrary optical carrier frequencies.

3 Key contributions

By noting that the rational approximation (1) computed via CVF can be decomposed into its in-phase and quadrature components, Sect. 4 discusses the derivation of the equivalent real-valued pole-residue representation, leading to a novel class of baseband photonic circuits. This novel class of circuit synthesis techniques starts directly from the rational approximation and complements the work of Ye et al. [23], which is restricted to state-space synthesis. Moreover, this approach bridges an important gap in adapting synthesis methods originally developed for electronic systems to baseband for PICs. The proposed pole-residue circuits are often more intuitive, as each element in the scattering matrix directly corresponds to an impedance element in the circuit. Additionally, in single-input multi-output (SISO) systems - such as demultiplexing filters - this approach can also offer enhanced computational efficiency [27].

Building on the wideband extension (4), obtained by shifting the poles of the rational model (1) along the imaginary axis, Sect. 5 proposes a parameterization of the baseband equivalent circuits with respect to wavelength. This approach yields wavelength-tunable equivalent circuits with a fixed topology, whose components values are parameterized with respect to the optical carrier frequency, and can be simulated at arbitrary wavelengths. Only a single model-building step is needed to create a model that can be practically used in a variety of settings.

Finally, Sect. 6 addresses the integration of third-party SPICE models with the proposed wavelength-tunable equivalent circuits. An interface circuit, which converts the complex phasor representation into equivalent voltages and currents, is defined to facilitate the interconnection with active and passive devices. By interconnecting active devices that accurately capture the electrical input and output impedances, intricate photonic–electronic co-simulation can be achieved. Moreover, the interface circuit accommodates the use of computationally cheap analytical models whose simplicity, accuracy, or parametric flexibility may offer benefits over the proposed wavelength-tunable equivalent circuit representations in certain scenarios. This methodology effectively combines the strengths of existing third-party SPICE models with the wavelength-tunable equivalent circuits, offering a versatile and scalable approach to photonic–electronic co-simulation.

4 Circuit synthesis from pole-residue form

In the literature, two distinct categories of circuit synthesis techniques can be identified: The first set of techniques computes a SPICE-equivalent circuit from the state-space form, while a second class of techniques starts from the pole-residue form. Though expressions for the real-valued state-space system are derived in [21], its equivalent pole-residue form is not defined. Consequently, only a subset of synthesis techniques can be adopted for the computation of equivalent circuit models representing baseband photonic scattering parameters. The circuit synthesis starting from pole-residue form is typically less efficient because of the large number of circuit components in series and in parallel [28], resulting in more complex equivalent circuits. On the other hand, the state-space approach requires numerous controlled sources, whereas the pole-residue representation can be synthesized as RLC circuits, which is typically more intuitive. To fill this gap, and allow the use of a broader class of circuit synthesis techniques [27, 29], the equivalent real-valued pole-residue form is here derived.

First, it is noted that the transfer function of the baseband equivalent system can be decomposed into its in-phase and quadrature components [30]

$$\begin{aligned}\mathbf{S}_l(s) &= \mathbf{S}_p(s) + j\mathbf{S}_q(s)\\ \mathbf{S}_p(s) &= \frac{\mathbf{S}_l(s) + \mathbf{S}_l^*(-s)}{2}\\ \mathbf{S}_q(s) &= \frac{\mathbf{S}_l(s) - \mathbf{S}_l^*(-s)}{2j}\end{aligned} \tag{5}$$

The baseband equivalent impulse response is then

$$\mathbf{s}_l(t) = \mathbf{s}_p(t) + j\mathbf{s}_q(t) \tag{6}$$

. It follows that the baseband backward traveling waves can be calculated as

$$\begin{aligned}\mathbf{b}_l(t) &= \mathbf{a}_l(t) * \mathbf{s}_l(t)\\ &= \big(\mathbf{a}_{\Re}(t) + j\mathbf{a}_{\Im}(t)\big) * \big(\mathbf{s}_p(t) + j\mathbf{s}_q(t)\big)\end{aligned} \tag{7}$$

Separating $\mathbf{b}_l(t)$ in its real and imaginary parts, the result above can be formulated as

$$\begin{aligned}\mathbf{b}_{\Re}(t) &= \mathbf{a}_{\Re}(t) * \mathbf{s}_p(t) - \mathbf{a}_{\Im}(t) * \mathbf{s}_q(t)\\ \mathbf{b}_{\Im}(t) &= \mathbf{a}_{\Re}(t) * \mathbf{s}_q(t) + \mathbf{a}_{\Im}(t) * \mathbf{s}_p(t)\end{aligned} \tag{8}$$

In the frequency-domain this yields

$$\hat{\mathbf{S}}_l(s) = \begin{bmatrix}\mathbf{S}_p(s) & -\mathbf{S}_q(s)\\ \mathbf{S}_q(s) & \mathbf{S}_p(s)\end{bmatrix} \tag{9}$$

Using relations (5), $\mathbf{S}_p(s)$ and $\mathbf{S}_q(s)$ can be expressed in pole-residue form

$$\begin{aligned}\mathbf{S}_p(s) &= \frac{1}{2}\sum_{k=0}^{K-1}\left(\frac{\mathbf{R}_k}{s-p_k} + \frac{\mathbf{R}_k^*}{s-p_k^*}\right) + \mathbf{D}\\ \mathbf{S}_q(s) &= \frac{j}{2}\sum_{k=0}^{K-1}\left(\frac{\mathbf{R}_k^*}{s-p_k^*} - \frac{\mathbf{R}_k}{s-p_k}\right)\end{aligned} \tag{10}$$

where $\mathbf{R}_k$ and p_k are the residue matrices and poles of the rational CVF model (1). Now, by combining expressions (10) and (9), it is easy to prove that

$$\hat{\mathbf{S}}_l(s) = \sum_{k=0}^{K-1}\frac{\hat{\mathbf{R}}_k}{s-p_k} + \frac{\hat{\mathbf{R}}_k^*}{s-p_k^*} + \hat{\mathbf{D}} \tag{11}$$

where $\hat{\mathbf{D}}$ is defined as in (2) and $\hat{\mathbf{R}}_k$ is given by

$$\hat{\mathbf{R}}_k = \begin{bmatrix}\mathbf{R}_k/2 & -j\mathbf{R}_k/2\\ j\mathbf{R}_k/2 & \mathbf{R}_k/2\end{bmatrix} \tag{12}$$

Expression (11) represents the real-valued pole-residue formulation that serves as a starting point for synthesis techniques such as those described in [27, 29], and allows the definition of the novel class of baseband pole-residue equivalent circuits.

5 Wavelength-tunable equivalent circuits

Since the synthesis technique presented in [23] requires the computation of a new CVF model and corresponding equivalent circuit for each value of the optical carrier frequency, it can become impractical for the modeling and simulation of multi-wavelength photonic systems. The wideband CVF models proposed in [24] address this issue by a parameterization with respect to the optical carrier frequency. However, the conversion of the wideband macromodel to a wavelength-tunable equivalent circuit is not yet discussed in the literature.

The wideband macromodel is obtained by shifting the anti-diagonal entries of $\hat{\mathbf{A}}$ by $2\pi\Delta f_c\mathbf{J}_m$. Instead of setting Δf_c to some desired value prior to computing the equivalent circuit, a more scalable and efficient strategy is to encode the dependency on Δf_c in the circuit's component values using SPICE math expressions. The latter approach will result in SPICE-compatible circuits that feature a fixed network topology, yet contain components whose values are adjusted as a function of the optical carrier frequency f_{cs}. Since the component values of the equivalent circuit are controlled by a single parameter, i.e., Δf_c, time-domain simulations at various wavelengths can be implemented through a straightforward parameter sweep. In this section, the conversion of the photonic baseband scattering parameters $\mathbf{S}_l(s)$ into a wavelength-tunable equivalent circuit is demonstrated. Within this framework, both the state-space approach presented in [23] and pole-residue approach presented here, are discussed.

Next, as demonstrated in [23], Neumayer's synthesis technique [31] can be adopted to convert the system of ODEs (4) into an equivalent circuit. Since only $\hat{\mathbf{A}}$ varies with Δf_c, the input–output network is not affected by the parameterization and only the internal states network will contain voltage-controlled current sources whose magnitude are a function of the optical carrier frequency. The internal states network constituting the equivalent circuit of a one-port scattering response is illustrated in Fig. 2. It is important to emphasize that all variables except for Δf_c are either constant or variables corresponding to the internal states of the equivalent circuit.

Starting from the pole-residue form (11), it is possible to adopt a new class of circuit synthesis techniques. Antonini et al. [29] propose a series RLC circuit in parallel with a voltage-controlled current source for the synthesis of a complex pole pair

$$F(s) = \frac{r}{s-p} + \frac{r^*}{s-p^*} \tag{13}$$

with $r = r_{\Re} + jr_{\Im}$ and $p = p_{\Re} + jp_{\Im}$. The equivalent circuit is illustrated in Fig. 3. Now, since the parameterization with

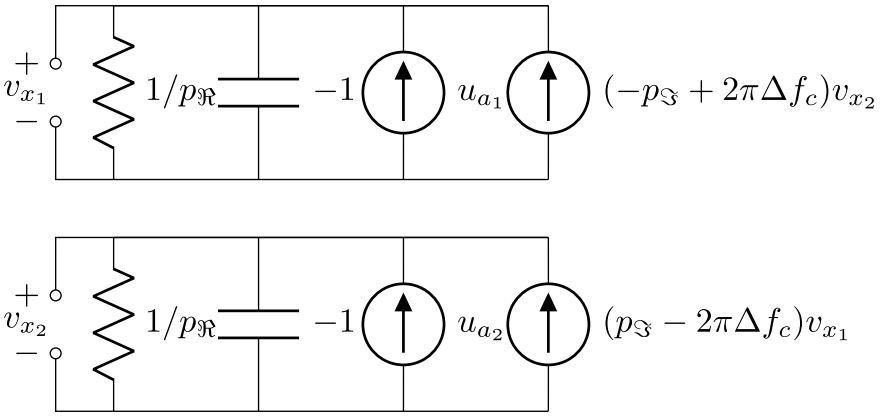

Fig. 2 The internal states network of a one-port scattering response modeled via CVF using a single pole $p = p_{\Re} + jp_{\Im}$

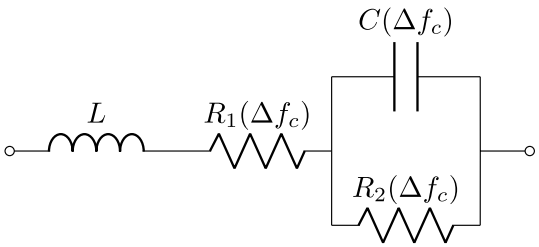

Fig. 3 Equivalent circuit for a complex pole pair [29]

respect to the optical carrier frequency is achieved by shifting the poles of the rational model by $j2\pi\Delta f_c$, L, R_1, C and R_2 are parameterized according

$$L = \frac{1}{2r_{\Re}} \tag{14}$$

$$R_1 = \frac{(p_{\Im} - 2\pi\Delta f_c)r_{\Im} - p_{\Re}r_{\Re}}{2r_{\Re}^2} \tag{15}$$

$$C = \frac{2r_{\Re}^3}{(r_{\Re}^2 + r_{\Im}^2)(p_{\Im} - 2\pi\Delta f_c)^2} \tag{16}$$

$$R_2 = \frac{-1}{C}\frac{r_{\Re}}{(p_{\Im} - 2\pi\Delta f_c)r_{\Im} + p_{\Re}r_{\Re}} \tag{17}$$

It follows that the optical carrier frequency of the wideband circuit can be easily adjusted by varying the R_1, R_2 and C parameters of the complex pole pair equivalent circuits.

6 Photonic–electronic co-simulation

This section presents a comprehensive framework for the simulation of complex systems comprising both passive and active components, along with driver and receiver electronics, within a unified SPICE-based environment. At the core of the framework is a standardized port interface that supports the integration of third-party behavioral models with the novel equivalent circuits. Linear passive devices can be modeled using the proposed wavelength-tunable equivalent circuits, while active and nonlinear passive devices are incorporated as third-party models. Such devices are treated in a modular, black-box fashion: the framework does not depend on the internal implementation of the device behavior, but only requires the specification of the input–output relationship at the ports, typically expressed in terms of amplitude and phase or optical power. Once defined, the model can be integrated through the port-conversion interface, facilitating seamless co-simulation of optical and electronic domains. In addition, the synthesis of wavelength-tunable equivalent circuits enforces passivity, ensuring numerically stable and physically consistent simulations even in the presence of nonlinear effects.

6.1 Port connectivity and model integration

The integration of third-party active and passive devices into the wavelength-tunable modeling framework necessitates a standardized approach to port connectivity. Other implementations of photonic models in SPICE use different conventions to represent ports and signal lines. One commonly-used implementation for optical connections in third-party models consists of a bus of multiple nets, each carrying either the baseband amplitude/phase or real/imaginary information traveling in a single direction [16]. Consequently, a single optical port quadruples in the SPICE circuit model: 2× for the two propagation directions and 2× to account for the

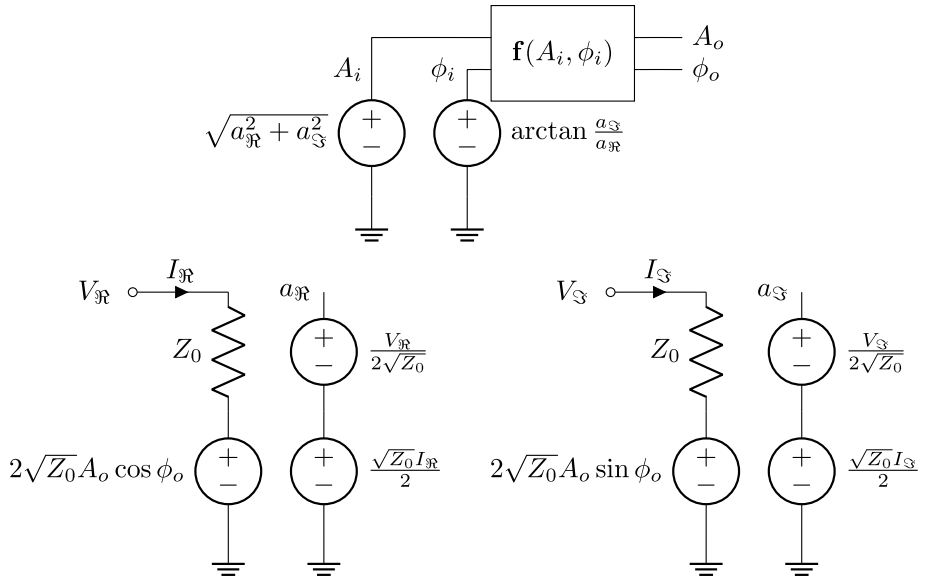

Fig. 4 Port conversion circuit for the interconnection with third-party models

complex nature of the signals. Since this port definition is not compatible with the equivalent voltage and current signals (3), third-party models cannot be directly connected to the wavelength-tunable SPICE equivalent circuits.

To facilitate interconnection with such third-party components, the port signals must be converted to an interface compatible with that illustrated in Fig. 1, while respecting the underlying physics of the SPICE simulation engine, such as Kirchhoff's Current Law (KCL) and Kirchhoff's Voltage Law (KVL). This can be achieved by adopting a similar circuit utilized for implementing the equivalent voltage and current (3), demonstrated in Fig. 4.

To prevent non-physical reflections caused by an impedance mismatch, the reference impedance Z_0 in the port conversion circuit must match the reference impedance used for generating the SPICE equivalent circuits. Additionally, the third-party models must be defined at the same baseband frequency used to configure the wavelength-tunable equivalent circuits.

6.2 Linear passive device models

While wavelength-tunable SPICE equivalent circuits excel in modeling the dynamic S-parameters of linear passive devices, analytic circuit models continue to play a vital role in photonic simulation due to their conceptual simplicity and computational efficiency. These models are particularly useful when exploring large design spaces, as they can often be parameterized directly with respect to layout dimensions, waveguide geometries, or substrate properties-something that is not currently feasible with the synthesized equivalent circuits. This makes analytic models indispensable in early-stage design exploration or layout-aware simulations, where rapid iteration is critical.

However, this modeling flexibility comes with limitations. Analytic models often rely on idealized assumptions and fail to properly capture the complex dispersive behavior exhibited by real-world devices. To overcome this, a divide-and-conquer strategy is recommended: devices showing strong dispersion over the wavelength range of interest are represented by the wavelength-tunable SPICE equivalent circuits, while other components, which exhibit well-behaved characteristics in terms of modeling, can be represented by compact analytic circuit models. Given that the computational runtime for CVF macromodeling and SPICE synthesis is small compared to that of full EM simulations, distinct SPICE equivalent circuits, applicable over a broad wavelength range, can be synthesized for each parameter configuration of interest. Alternatively, a parametric CVF macromodel, as proposed in [24], can be computed to serve as the starting point for the SPICE synthesis.

One important constraint for using analytic models in this framework is that they must support bidirectional signal flow, as passive devices are typically embedded deeply within the optical path, where light can propagate in either direction. Proper handling of this bidirectionality is essential for accurately capturing physical phenomena such as backscattering, back-reflections and resonant effects-especially in feedback-sensitive structures like ring resonators or interferometers. Without this capability, signal reflections-modeled by the novel wavelength-tunable equivalent circuit-would simply get lost as the signal propagates

through the system, compromising the accuracy and fidelity of the overall circuit simulation.

6.3 Active or nonlinear passive device models

Active components-including lasers, modulators, semiconductor optical amplifiers (SOAs), and photodetectors-serve as the key interfaces between the electrical and optical domains. These devices can be broadly classified into two categories. The first includes peripheral components like lasers and photodetectors, which typically operate in a unidirectional manner and are modeled using input–output transfer characteristics. In this case, the port conversion circuit inherently provides proper termination of the equivalent circuit, even when signal propagation occurs in only one direction. The second category comprises quasi-static tuning elements, such as phase shifters and electro-optic modulators, which are embedded directly within the signal path. Unlike peripheral devices, these components must support bidirectional optical propagation, similar to passive elements. The same considerations apply to nonlinear passive devices, which must also support bidirectional optical propagation when embedded within the signal path.

The fidelity of the active device models significantly impacts the overall accuracy of the photonic–electronic co-simulation. Although their optical interfaces closely resemble those of passive components, active components are characterized by an electrical interface that must be modeled with care. In particular, accurately capturing the electrical input and output impedances is essential for intricate co-simulation with driver and receiver electronics. Any mismatch or misrepresentation can result in signal reflections and distortions, adversely affecting both the electronic circuitry and the optical signal integrity. These effects can significantly degrade the reliability of the overall co-simulation and must be carefully accounted for. In scenarios where the electrical control signals are slowly varying-such as in programmable photonics or actively tuned filters-modeling the device's response time through a simple RC delay is often sufficient to capture the relevant dynamic behavior.

Simplified behavioral models, particularly of modulators and photodetectors, are often linearized around a fixed bias point, in which small-signal electrical modulation is directly mapped to variations in optical output power. In such models, the electrical AC signal is converted into an optical power fluctuation, typically neglecting any phase modulation effects. This assumption is valid when the modulator operates in a regime where the modulation index is small, the optical phase remains constant, and only intensity modulation is of interest. Under this condition, the optical carrier can be expressed as $A(t)e^{j\omega t+j\phi(t)}$ where $\phi(t)=0$, indicating the absence of phase modulation. As a result, such models output optical power rather than complex amplitude and cannot be directly interfaced using the port conversion circuit shown in Fig. 4, which requires access to the optical amplitude. Instead, the optical power must first be converted into an equivalent amplitude representation. Assuming no phase modulation, the total optical power is related to the amplitude by

$$P_{tot} = (A_{dc} + A_{ac})^2 = P_{dc} + P_{ac} \tag{18}$$

where $P_{dc} = A_{dc}^2$ is the optical output power at the fixed bias point and $P_{ac} = A_{ac}^2 + 2A_{dc}A_{ac}$ is the simulated AC power. It follows that the AC amplitude, which needs to be passed to the port conversion circuit, is obtained as $A_{ac} = \sqrt{P_{ac} + P_{dc}} - \sqrt{P_{dc}}$. It is important to note that this conversion necessitates prior knowledge of the DC optical power at the linearization point, as it is essential for accurately recovering the optical amplitude from the AC power (Fig. 5).

6.4 Multi-wavelength simulation

The wideband SPICE equivalent circuits can be simulated at arbitrary optical carrier frequencies by sequentially adjusting the parameter Δf_c. Any wavelength dependence of third-party active or passive device models can be incorporated indirectly by expressing their behavior as a function of this parameter. Multi-wavelength system analysis is then performed by simulating multiple instances of the circuit, each corresponding to a specific wavelength channel.

This strategy assumes that the response of each device at a given wavelength depends exclusively on the optical input signals at that wavelength; however, this assumption does not always hold, and special care is required, particularly when dealing with nonlinearities. Active photonic components, such as semiconductor optical amplifiers (SOAs), can induce cross-wavelength interactions arising from gain saturation, carrier dynamics, or chirp-induced spectral broadening. In such cases, the optical signals from all channels must be known simultaneously at each time step, which is not supported by this simulation scheme. Moreover, the receiver electronics operate directly on the total

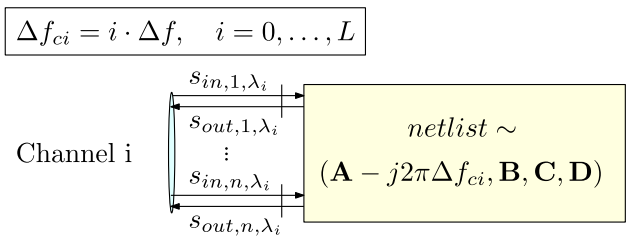

Fig. 5 SPICE simulation of multiple instances of the equivalent circuit, each corresponding to a specific wavelength channel

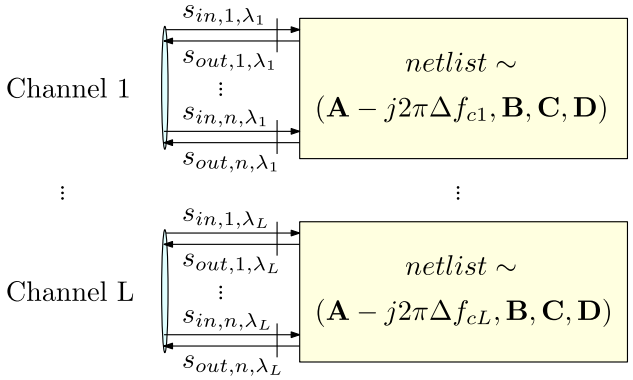

Fig. 6 SPICE equivalent circuit model where each wavelength channel is assigned a distinct logical port

photocurrent, including the contributions from all wavelength channels. As a result, this scheme is applicable only when both the optical devices and the receiver electronics can be adequately described by small-signal models. This scheme will be denoted as the Small-Signal Representation (SSR).

An alternative approach, illustrated in Fig. 6, which does not impose this limitation, involves assigning input signals at different wavelengths to separate logical ports. Consequently, the equivalent circuit model of an n port device, supporting L different wavelengths channels, will end up having nL logical ports. In the particular case of the wideband CVF macromodeling framework, this is achieved by setting Δf_c according to the various wavelength channels of the PIC and aggregating the resulting models into an overall equivalent representation with a port interface as illustrated in Fig. 6. This approach ensures that the optical signals from all channels are simultaneously available at each simulation time step, thus allowing accurate computation of the outputs of nonlinear components. Since this scheme enables accurate simulation of nonlinearities in a multi-wavelength context, it will be referred to as the large-signal representation (LSR). As each wavelength channel introduces an additional set of ports and corresponding circuit elements, the size of the modified nodal analysis (MNA) matrix in the SPICE simulation increases significantly. Although the overall system complexity scales linearly with the number of wavelength channels, the resulting matrix size and memory requirements can grow rapidly, particularly in circuits with numerous interconnections or large numbers of nonlinear and active components. However, when portions of the circuit are decoupled-such as interconnected passive subcircuits corresponding to different wavelength channels-the resulting MNA matrix remains highly sparse. This sparsity arises because only a small fraction of nodes are coupled across channels, while most connections remain local to each subcircuit. Many SPICE solvers efficiently exploit this sparsity through specialized sparse matrix algorithms, minimizing both computational runtime and memory usage. Although the LSR scheme offers clear advantages, its main drawback is that the circuit must be duplicated for each wavelength channel, resulting in a rapid increase in schematic size and complexity. Consequently, managing such multi-channel configurations becomes cumbersome in standard circuit simulators, such as LTspice. A potential solution would be to develop a software interface or API that automatically generates and manages the multi-channel netlists using simulation backends such as NGspice. However, the development of such software tool is beyond the scope of the present work.

7 Numerical results

In this section, three application examples of the proposed modeling framework are presented. Transient simulations of the wavelength-tunable equivalent circuits are conducted using LTspice, a freely available and widely used SPICE circuit simulator. The modeling and numerical simulations are carried out on a personal computer equipped with an Intel Core i7 processor and 16 GB of RAM. Throughout all experiments, the reference impedance of the equivalent circuits is set to 50 Ω. The wavelength-tunable equivalent circuits, synthesized starting from the pole-residue representation, are referred to as PR netlists, those synthesized from the state-space representation, are referred to as SS netlists. The accuracy of the transient simulations is evaluated using the time-averaged root-mean-square error (RMSE) relative to the reference method, computed across all output ports and time steps as

$$\mathrm{RMSE} = \sqrt{\frac{1}{N}\sum_{p}\sum_{t}\left(y_{t,p} - y_{t,p}^{\mathrm{ref}}\right)^2}, \tag{19}$$

where $y_{t,p}$ and $y_{t,p}^{ref}$ denote the simulated and reference outputs, respectively, at port p and time step t, and N denotes the number of samples.

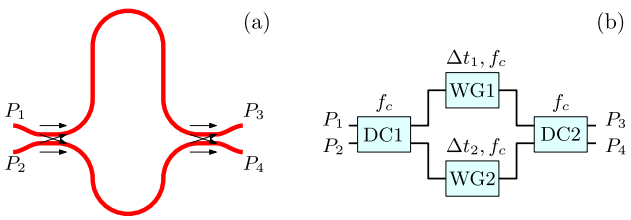

Fig. 7 MZI: Top view of the lay-out (**a**) and a hierarchical schematic (**b**) of the balanced MZI

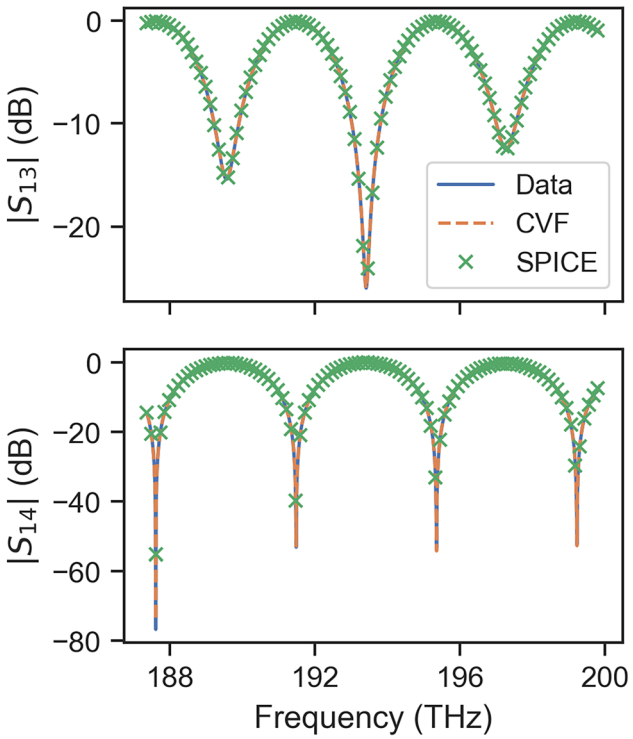

Fig. 8 MZI: Simulated transmission spectrum of the balanced MZI (blue), fit by the CVF macromodel (orange) and reconstructed spectrum with the hierarchical PR wavelength-tunable equivalent circuit (green)

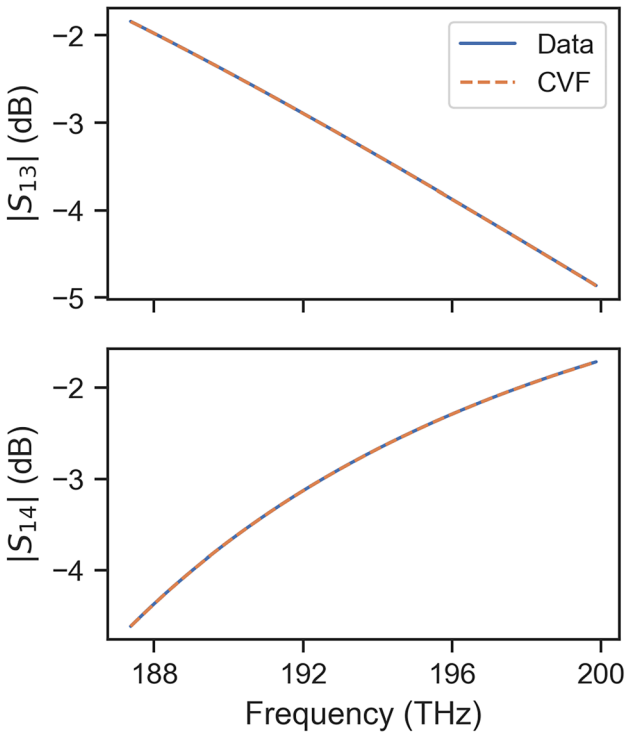

Fig. 9 MZI: Simulated transmission spectrum of the DC (orange) and the fit by the CVF macromodel (blue)

7.1 Mach–Zehnder interferometer - MZI

In this first example, a balanced *Mach-Zehnder interferometer* (MZI) functioning as a wavelength filter is studied. The MZI structure comprises two S-bend *directional couplers* (DCs) and two waveguides, forming its upper and lower arms, as shown in Fig. 7. While photonic–electronic co-simulation is not considered in this example, the objective is to compare hierarchical and flat modeling strategies for the simulation of passive photonic circuits. This case study illustrates how structural modeling choices influence simulation workflow, modularity, and reusability. Furthermore, it demonstrates how the proposed divide-and-conquer methodology enables the integration of wavelength-tunable equivalent circuits for dispersive components alongside analytic models for parameterized, idealized behavior.

The waveguides of the MZI are modeled as lossless non-dispersive devices with a constant group delay. Their forward transmission in the frequency domain can be expressed as

$$S_{WG}(\omega) = e^{-j\omega\Delta t} \tag{20}$$

where $\Delta t = Ln_g/c$ is the optical delay in the waveguide, n_g is the group index, L is the length of the waveguide and c is the speed of light. In this example, the delays of the upper and lower waveguide arms are set to $\Delta t_1 = 1.06\,\text{ps}$ and $\Delta t_2 = 0.80\,\text{ps}$, respectively, resulting in a $\pi/2$-length difference at the filter wavelength of 1.55 μm. The S-bend DCs, designed for a 50:50 coupling ratio at 1.55 μm, are simulated in the eigenmode expansion (EME) solver from ANSYS Lumerical.

An initial approach for modeling the balanced MZI is to treat it as a black-box device with scattering parameters as shown in Fig. 8. Using the Luceda design software IPKISS, the scattering parameters of each individual component are combined into a single overall S-matrix that describes the propagation through the MZI. Subsequently, this overall S-matrix is evaluated at 1001 equidistant frequency samples in the frequency range [187.37; 199.86] THz (corresponding to a wavelength of [1.5; 1.6] μm). Next, a wideband CVF macromodel with 31 poles is computed, yielding an accuracy, defined as the maximum error between the data and the model, of -50 dB. The baseband frequency shift is arbitrarily chosen at $f_c = 194.67$ THz. A standard bottom-up approach is used to select the required number of poles [32]. Finally, following the procedure outlined in this work, two wavelength-tunable equivalent circuits are computed: one derived from the state-space representation and the other from the pole-residue representation (Fig. 9).

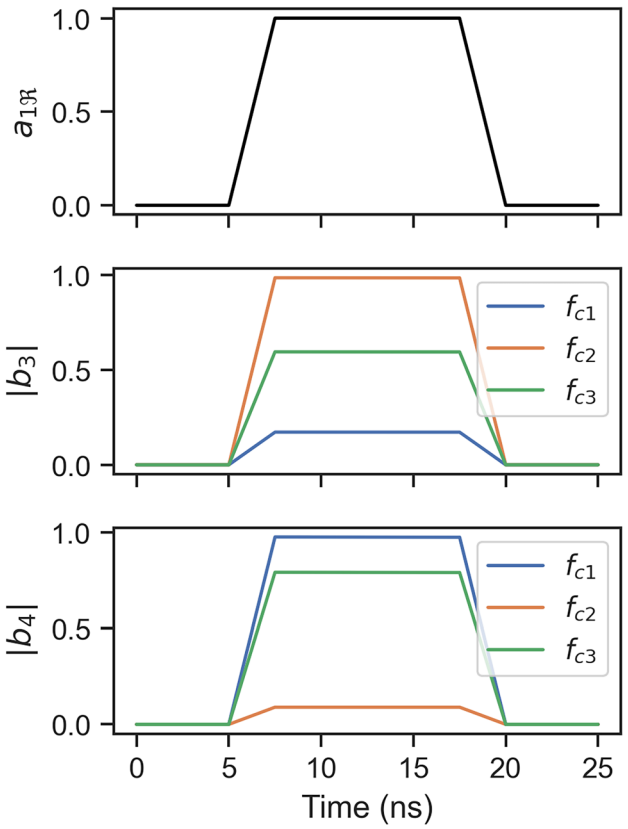

Fig. 10 MZI: Transient response obtained with the hierarchical PR wavelength-tunable equivalent circuit at baseband center frequencies $f_{c1} = 189.6$ THz, $f_{c2} = 191.6$ THz and $f_{c3} = 194.2$ THz

An alternative approach to the one previously discussed involves the definition of separate circuit models for the DCs and the waveguides. These models can then be interconnected in a hierarchical circuit representing the balanced MZI, see Fig. 7 (b). It should be noted that while S_{14} in Fig. 8 resembles the standard frequency response of a balanced MZI, this is not applicable to S_{13}. This discrepancy arises from the wavelength-dependent power coupling of the symmetric DCs and their specific arrangement within the MZI. It is crucial to note that analytic DC models, which assume constant power coupling across wavelength as presented in [16], do not adequately capture this behavior. In this context, a wavelength-tunable equivalent circuit is computed for the 50:50 DC, while an analytic circuit model is implemented for the waveguides. This strategy ensures accurate modeling of the dispersive scattering parameters of the DCs, while allowing for a parametric and computationally efficient circuit model to represent the waveguides. The primary advantage of this approach lies in its flexibility. The individual components can be reused and rearranged in various configurations, allowing for greater adaptability in circuit design.

Table 1 MZI: Benchmark results

Netlist	Topology	RMSE	CPU time (s)
SS	Hierarchical	2.0e−4	82.7
SS	Flat	6.8e−5	50.5
PR	Hierarchical	1.6e−4	487.6
PR	Flat	4.0e−5	389.4

Starting from the frequency domain response (20) of the non-dispersive waveguide, an equivalent time-domain model can be formulated as

$$\begin{aligned} A_o(t) &= A_i(t - \Delta t) \\ \phi_o(t) &= \phi_i(t - \Delta t) + 2\pi\Delta t f_c \end{aligned} \tag{21}$$

with A_i and A_o the amplitude and ϕ_i and ϕ_o the phase of the incoming and outgoing optical waves, respectively. The scattering response of the DC is simulated at 201 equidistant frequency samples in the frequency range [187.37; 199.86] THz. Starting from this dataset, a wideband CVF macromodel with 10 poles and an accuracy of -58 dB is computed. Then, the system of ODEs, governed by the CVF macromodel, is converted into an equivalent SS and PR netlist.

To verify that the baseband frequency of the wavelength-tunable equivalent circuits is properly configured by setting the parameter Δf_c within the SPICE simulator, the following experiment is conducted: The equivalent circuits of the directional coupler and MZI are imported in LTspice and terminated with matched resistors. Then, a transient simulation is performed by applying a trapezoid pulse to the in-phase component of port P_1. Since the scattering parameters of the MZI are approximately constant over the bandwidth of the input signal, the steady-state in-phase and quadrature outputs of the MZI, directly map to the real and imaginary part of the corresponding scattering parameter in the frequency domain. Thus, by iteratively adjusting the baseband frequency and performing a time-domain analysis, it becomes possible to reconstruct the scattering response of the device.

Figure 8 shows the reconstructed spectrum, obtained from 201 transient simulations in SPICE, conducted at uniformly spaced center frequencies across the modeling range. The transient simulation results at several baseband center frequencies are illustrated in Fig. 10. Note that the simulated forward and backward traveling waves are derived from the SPICE voltage and current signals via the expressions (3). The accuracy of the wavelength-tunable equivalent circuits, defined as the root mean square error (RMSE) relative to the simulation of the complex-valued ABCD model using *lsim*, averaged over the 201 simulation runs, is reported in Table 1, along with the total CPU time. These results indicate that the transient responses obtained with wavelength-tunable equivalent circuits converge very well with

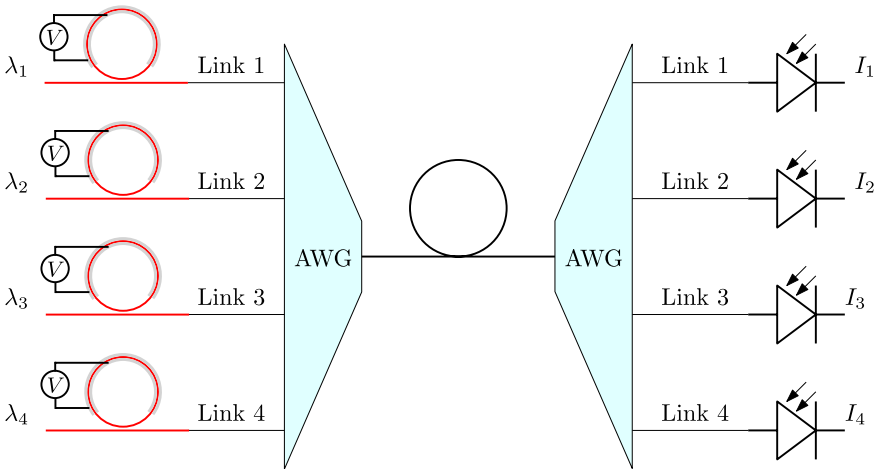

Fig. 11 WDM: Functional diagram of the WDM system

the reference simulation. Furthermore, the hierarchical circuit created by interconnecting the wavelength-tunable equivalent circuits is simulated with the analytic waveguide model. These are connected via the port conversion circuit shown in Fig. 4. The simulation confirms that both KCL and KVL are satisfied, ensuring accurate results. Although an analytic model for a waveguide was used in this study, the same approach can be applied to any active or passive third-party model.

7.2 Wavelength division multiplexing system - WDM

This numerical example presents the characterization of the WDM system, including driver and receiver electronics, ring modulators and arrayed waveguide gratings, as illustrated in Fig. 11. This discussion includes a comparison and benchmarking of the developed simulation methodologies, an analysis of electrical driver characteristics on the eye pattern of a 25 Gbaud PAM-4 transmission scheme, a characterization of the output voltage nonlinearity introduced by driver and receiver electronics, and an evaluation of inter-channel crosstalk on overall system performance.

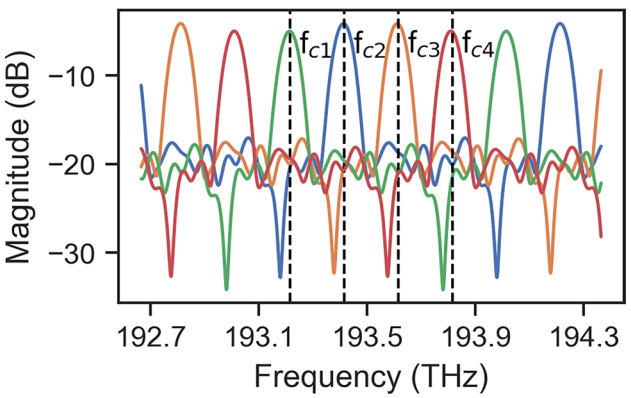

Fig. 12 WDM: Transmission spectrum of the 4-channel AWG

Both the multiplexer and demultiplexer within the WDM system are implemented by the same 4-channel arrayed waveguide grating (AWG) studied in the authors' previous work [24]. Its transmission spectrum is illustrated in Fig. 12. The data generation and model computation, as detailed in [24], result in a stable and passive CVF macromodel with 24 poles. This model yields an accuracy, defined as the maximum error between the data and the model response, of −61 dB. A standard bottom-up approach is used to select the required number of poles [32]: the initial number of poles is iteratively increased until the desired accuracy is reached. Then, starting from the complex-valued rational representation (1), the equivalent real-valued pole-residue and state-space representations are derived. This, in turn, facilitates the computation of two wavelength-tunable equivalent circuits comprising the parameterized controlled sources and RLC elements presented here. These circuits can be used to perform time-domain simulation at arbitrary optical carrier frequency in the range [193.01 + $BW_{mod}/2$; 194.01 - $BW_{mod}/2$] THz, where BW_{mod} is the modulation bandwidth (Fig. 14).

A linear equivalent circuit model, as presented in [9], is employed for the depletion-type silicon microring modulator (MRM). The model comprises three primary blocks: (1) parasitic elements arising from interconnects and contact pads, (2) the electrical representation of the core p–n junction, and (3) a lossy LC tank circuit capturing the optical modulation behavior of the silicon MRM. The model parameters, derived from experimental data of a fabricated silicon MRM device, are taken from [9]. It is assumed that these parameter values remain constant across the wavelength range of the WDM system; hence, the same model is used for modulation of all four optical carriers. Although not pursued in this

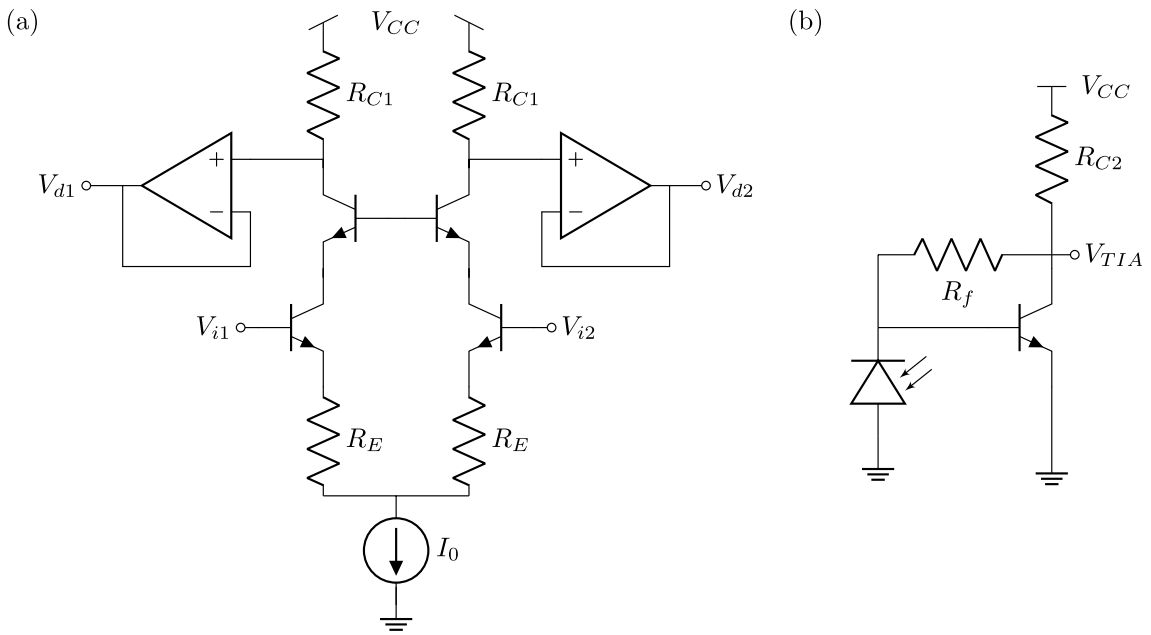

Fig. 13 WDM: Simplified schematics of the differential cascode driver circuit (left) and the common-emitter transimpedance amplifier (right)

Fig. 14 WDM: Schematic diagram of the microring modulator linearized circuit model

study, large-signal models could also be adopted for the ring modulators (e.g., [8]) without requiring any modifications to the overall modeling approach.

The electronic driver and readout circuits, depicted in Fig. 13, are implemented using a differential cascode common-emitter configuration and a transimpedance amplifier (TIA) based on a common emitter stage, respectively. Both stages are modeled using the standard NPN transistor model from LTspice. The outputs of the differential cascode are buffered to provide sufficient drive for the ring modulators. In practice, this stage could be implemented, for example, using an NMOS source follower; however, for simplicity, it is modeled here as an ideal non-inverting op-amp.

Both the Small-Signal Representation (SSR) and Large-Signal Representation (LSR) strategies are evaluated and compared. In the SSR approach, a separate simulation is launched for each wavelength channel, whereas in the LSR approach, signals corresponding to different wavelength channels are assigned to distinct logical ports. Since each wavelength channel is driven by an independent circuit (differential cascode driver with ring modulator) and the optical path contains no nonlinear devices, the simulated optical signals are equivalent under both strategies. The primary distinction between the two schemes lies in the simulation of the receiver electronics. In the LSR strategy, the total photocurrent arising from all wavelength channels is computed at each time step, thus enabling large-signal analysis and accurate modeling of nonlinear effects in the receiver. Conversely, the SSR strategy computes the photocurrent for each channel through separate simulations and adopts a linearized TIA model, thereby restricting the analysis at the receiver side to the small-signal regime.

In both SSR and LSR schemes, the photocurrent is injected into the electronic readout circuit via a behavioral current source. This effectively decouples the receiver electronics from the driver and optical transmission system. Consequently, validation and comparison can be performed at the optical signal level; once the optical waveforms are verified, correct simulation of the receiver electronics in the small-signal (SSR) or large-signal (LSR) regime is guaranteed.

To assess the accuracy of the proposed co-simulation schemes, two benchmark methodologies are considered. In the first approach, the microring modulators and the driver electronics are simulated independently in SPICE. The resulting output waveforms are exported and applied as input excitations to a behavioral CVF macromodel, which is evaluated using the *lsim* function in Python. This co-simulation methodology serves as a benchmark, as both the equivalent model of the ring modulator and the CVF macromodels have been independently verified.

The second strategy is a variation of the first, but replaces the dynamic CVF model with a static, instantaneous

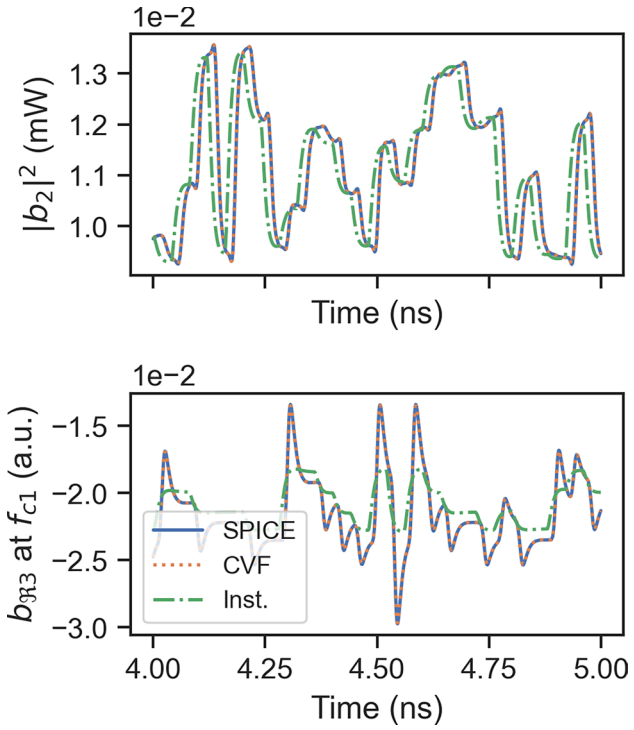

Fig. 15 WDM: Comparison of transient responses obtained using SPICE-based, CVF-based, and instantaneous (Inst.) simulation methodologies

approximation. In this case, signal magnitude and phase are adjusted according to the system's scattering parameters evaluated at the central wavelength of each optical carrier. This method corresponds to the default time-domain model used for passive devices in Caphe, the photonic circuit simulator developed by Luceda Photonics [33]. These two benchmarks strategies are referred to as the CVF-based and instantaneous (Inst.) methods, respectively. Finally, unless stated otherwise, the optical input power is fixed at 1dBm in all experiments.

A transient simulation of the entire WDM system is performed by applying four 25 Gbaud PAM-4 signals (50 Gbs per channel) $u_i(t)$, $i = 1, \ldots, 4$ at the inputs of the differential driver. These signals are modulated at optical carrier frequencies $f_{ci} = 193.05\,\text{THz} + i \cdot 200\,\text{GHz}$, which are offset by 40 GHz from the center wavelengths of the AWG channels. The WDM system is simulated over 8 ns, corresponding to 200 symbols. By opting for the PAM-4 modulation scheme, the signal detection is performed incoherently. Consequently, the total signal power at an AWG output port can be obtained by summing the powers of the individual signals simulated at the different optical carrier frequencies.

Figure 15 shows the total transmitted optical power at link 1 and the in-phase component of the transmitted signal with optical carrier frequency f_{c1} at link 3. The accuracy of the various simulation methodologies, calculated as the RMSE of the optical outputs relative to the CVF-based benchmark strategy, is reported in Table 2, along with the total CPU time. Both the SSR and LSR SPICE co-simulation schemes demonstrate strong agreement with the reference output, as evidenced by the low RMSE. These results confirm the accuracy of the wavelength-tunable equivalent circuits and validate the interconnection strategy based on the port conversion circuits. In contrast, the instantaneous model fails to accurately capture all transient effects. This discrepancy arises primarily for two reasons: First, the optical carriers are located near the edges of the AWG passbands, where the spectral response is no longer flat across the signal bandwidth, thereby violating the instantaneous model's assumption of a non-dispersive spectral profile. Second, the instantaneous model neglects the group delay introduced by the two AWGs, an effect that becomes critical when simulating the transient behavior of many photonic–electronic integrated systems.

Table 2 WDM: Benchmark results

Netlist	Scheme	RMSE	CPU time (s)
SS	LSR	1.8e−5	239
SS	SSR	2.4e−5	402
PR	LSR	2.95e−5	1212
PR	SSR	2.4e−5	3264
Inst	/	2.8e−3	23

As motivated in [28], traditional pole-residue synthesis techniques, such as the one used in [29], are generally less efficient compared to state-space methods. This inefficiency arises from the high number of circuit components arranged in series and parallel configurations, leading to a larger MNA system matrix. Consequently, computational runtimes increase, as confirmed by the CPU times reported in Table 2. Alternative pole-residue topologies have been proposed [27]; however, these are not explored here as they fall outside the scope of this study.

With both the SSR and LSR schemes validated at the optical level, their performance at the receiver side is now compared. Owing to inter-channel crosstalk resulting from the finite stopband rejection of the AWGs, the photodiode current includes contributions from multiple wavelength channels. When the receiver operates within its linear regime, both approaches yield consistent small-signal results. However, as the TIA enters saturation and nonlinear effects start to dominate, only the LSR approach, which accurately models large-signal behavior, remains accurate.

This effect is demonstrated by an experiment in which two optical carriers at 193.45 THz and 194.65 THz are injected into link 1 and link 2 of the WDM system, respectively. The first carrier is held at constant power such that the output voltage of the TIA in link 1 is biased near half of

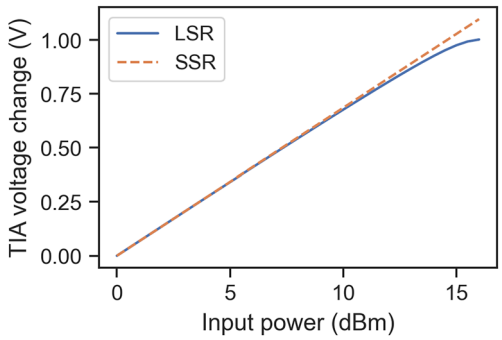

Fig. 16 WDM: Simulated TIA voltage change versus increasing optical input power, obtained with SSR and LSR schemes

its voltage swing, while the power of the second carrier is swept. Due to the finite stopband attenuation of the AWGs, a fraction of the 194.65 THz carrier leaks into link 1 and manifests at its TIA output. The resulting increase in TIA voltage, caused by this leakage and shown in Fig. 16, highlights the onset and impact of nonlinear distortion at the receiver side. At low input powers, both modeling schemes yield consistent results, whereas at high photocurrents, the compression observed in the receiver is captured only by the LSR scheme. For this reason, and to enable determination of the DC operating point, all simulations in the following experiments are performed using the LSR scheme.

The differential driver's electrical properties strongly affect the high-speed performance of the WDM system. Of particular importance is the emitter degeneration in the differential pair, which is introduced via the emitter resistance R_E. The presence of R_E provides local negative feedback, which linearizes the electrical driver's gain characteristic and suppresses distortion. At the same time, however, R_E reduces the effective transconductance, thereby lowering the available gain and limiting the power delivered to the ring modulator. If R_E is chosen too small, the driver operates with high transconductance but exhibits strong nonlinear distortion, which degrades the signal integrity and results in eye closure. Conversely, if R_E is made excessively large, the driver achieves excellent linearity but insufficient gain, resulting in a degraded modulation depth and a reduced eye opening. These effects are illustrated in Fig. 17, which shows the simulated eye diagrams at link 4, obtained from the TIA output, for different values of R_E. The results suggest that an emitter resistance in the range of $150 - -200\,\Omega$ offers a good trade-off between linearity and gain.

In the next experiment, the nonlinearity of the WDM system is characterized with the emitter resistance set to $R_E = 200\,\Omega$. Unlike conventional methodologies that separately model the electrical and optical subsystems, the proposed framework facilitates a comprehensive analysis of the entire photonic–electronic system within a unified simulation environment.

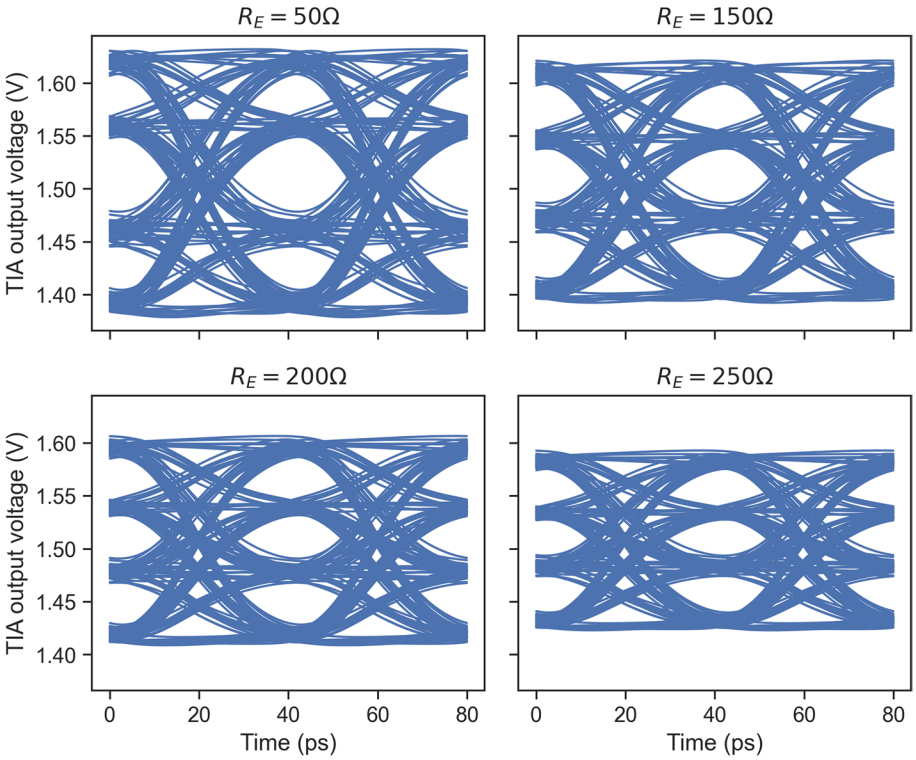

Fig. 17 WDM: Eye-diagram analysis at port 4 obtained for different values of the emitter resistance R_E

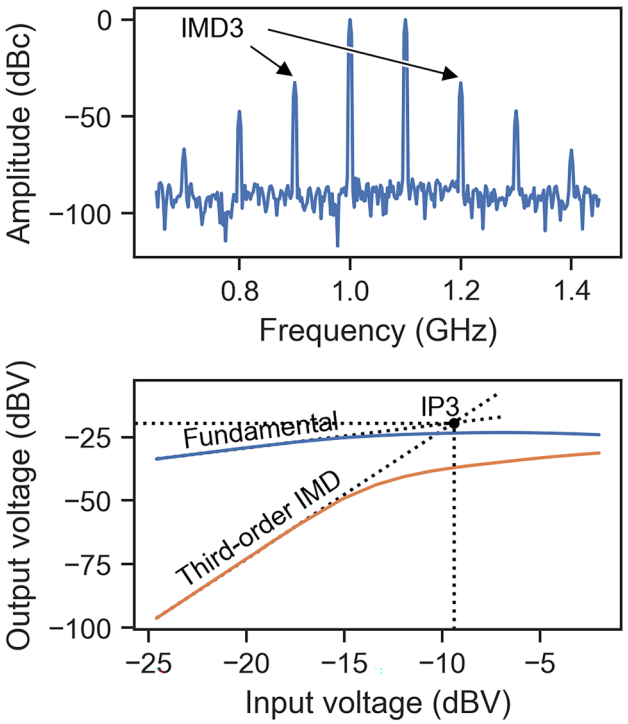

Fig. 18 WDM: Results of the two-tone test. (Left) Optical spectrum measured at the TIA output. (Right) Variation of the fundamental and IMD3 responses with the input amplitude of the two tones

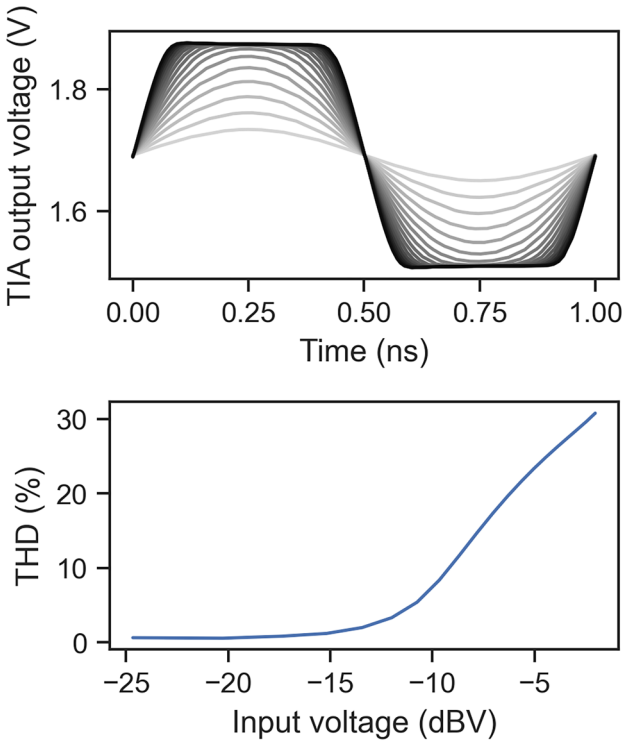

Fig. 19 WDM: Effect of nonlinear distortion on the TIA output: (left) time-domain waveforms illustrating the transition from a sinusoidal to a square-like output with increasing amplitude of the input tones, and (right) THD as a function of input tone amplitude

To quantify the nonlinear behavior observed at the TIA output, both the third-order intercept point (IP3) and the total harmonic distortion (THD) are evaluated. The IP3 parameter provides a measure of the relative strength of third-order intermodulation products generated when two closely spaced input tones propagate through a nonlinear system. In this experiment, two electrical tones at 1.0 GHz and 1.1 GHz were injected while monitoring the output voltage of link 1. The 100MHz frequency offset between the tones produces a beating envelope with a 10ns period in the optical waveform. The corresponding optical spectrum, shown in Fig. 18, exhibits distinct third-order intermodulation (IMD3) products at 0.9 GHz and 1.2 GHz. The IMD3 as a function of electrical input voltage is plotted in Fig. 18. The IP3 is determined from the linear extrapolation point at which the fundamental and third-order intermodulation responses intersect.

THD, on the other hand, quantifies the relative contribution of harmonic components to the fundamental tone and serves as an indicator of waveform distortion. In SPICE, THD is computed by injecting a single-tone input at 1.0 GHz while analyzing the harmonic content of the TIA output. As the input voltage increases, the initially sinusoidal output gradually transitions toward a square-like waveform, as illustrated in Fig. 19, reflecting stronger harmonic generation and increased nonlinear distortion.

7.3 Programmable photonics - FPGA

This numerical example demonstrates the applicability of the proposed framework in the context of programmable photonics. Since 2013, when the concept of a universal photonic circuit was first proposed [9], researchers have been working on photonic integrated circuits that can be reconfigured to perform different functions. On such chips, light is routed through waveguides, which are coupled together using electrically controlled 2×2 photonic gates. In these gates, light from two waveguide inputs is mixed (in a linear combination) into two outputs. Such photonic gates, can be cascaded into a network or mesh of waveguides, and the flow of light is controlled electronically by setting the actuation voltage or current of the gates.

The tight integration of electronics and photonics in these systems presents significant challenges in modeling and simulation. Traditional approaches typically simulate the electrical control circuits using EDA tools, while the photonic mesh is simulated using specialized PDA tools, often using simplified analytical models for the couplers. In contrast, the proposed framework enables the simulation of both the electronic and photonic circuitry within a unified

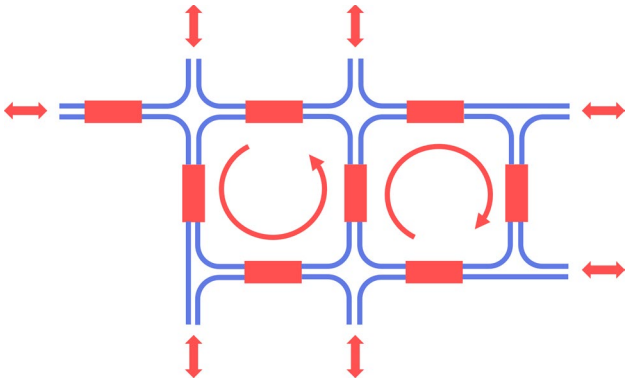

Fig. 20 FPGA: The programmable waveguide mesh composed of square cells. The red rectangles represent the 2×2 analog gates

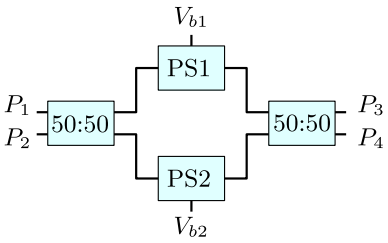

Fig. 21 FPGA: Hierarchical schematic of the 2×2 analog gate, constructed using two splitters (50:50) and phase shifters (PS)

SPICE environment, providing a more comprehensive and accurate representation of the system's behavior.

A photonic FPGA, composed of a small number of rectangular mesh cells is illustrated in Fig. 20. Within this structure, each analog gate - depicted as a red rectangle in Fig. 20 - is implemented by an MZI. Each MZI is, in turn, constructed using two 2×2 splitters with phase shifters placed in its upper and lower arms, as illustrated in Fig. 21. By applying appropriate bias voltages to these phase shifters, the 2×2 gate can be configured to achieve the desired power coupling and phase shift. In total, the mesh contains 8 analog gates, corresponding to 16 splitters and 16 phase shifters.

In this numerical example, the mesh is configured to operate as a flat-top filter. In particular, the analog gates in Fig. 20 are programmed to form a double-ring resonator. The equivalent circuit of the double-ring filter is illustrated in Fig. 22. Inside the rings, the analog gates (green blocks) operate in bar mode and control the optical round-trip length, which determines the resonance frequency of the filter. The power coupling coefficients of the analog gates, configured as tunable couplers (yellow blocks), are selected to achieve a second-order Butterworth response. Furthermore, the analog gate at the input acts as a combiner, enabling the injection

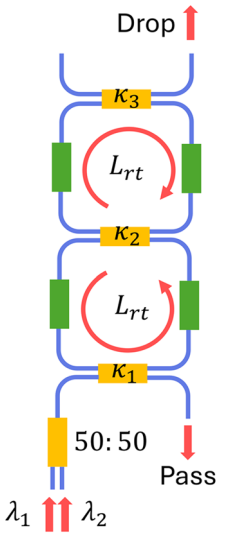

Fig. 22 FPGA: The equivalent double-ring flat-top filter. Green blocks denote analog gates set to bar mode, functioning as waveguides; yellow blocks denote analog gates configured as directional couplers

of two optical signals-delivered via separate ports-into the double-ring filter structure.

The two 50:50 couplers of the MZI's are implemented using a compact 2×2 splitter, whose transmission characteristics are shown in Fig. 23. The scattering parameters of this device are obtained through FDTD simulations using Ansys

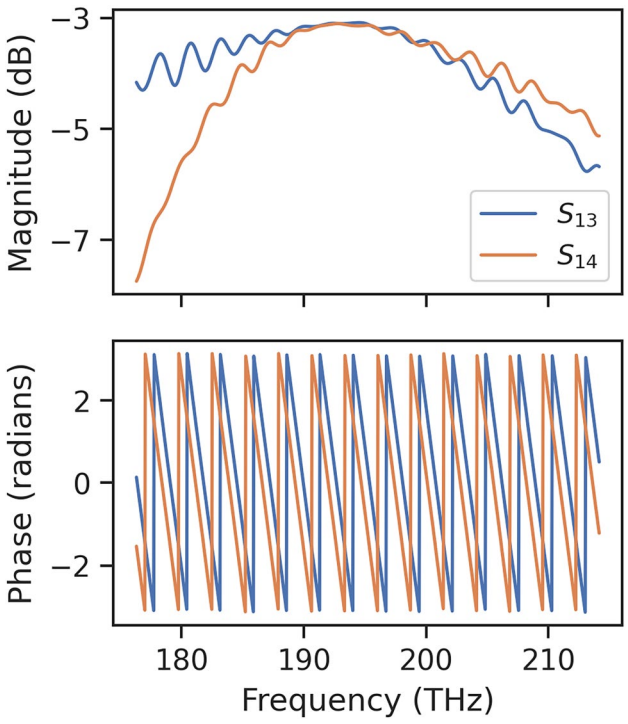

Fig. 23 FPGA: Transmission characteristics of the compact 2x2 splitter

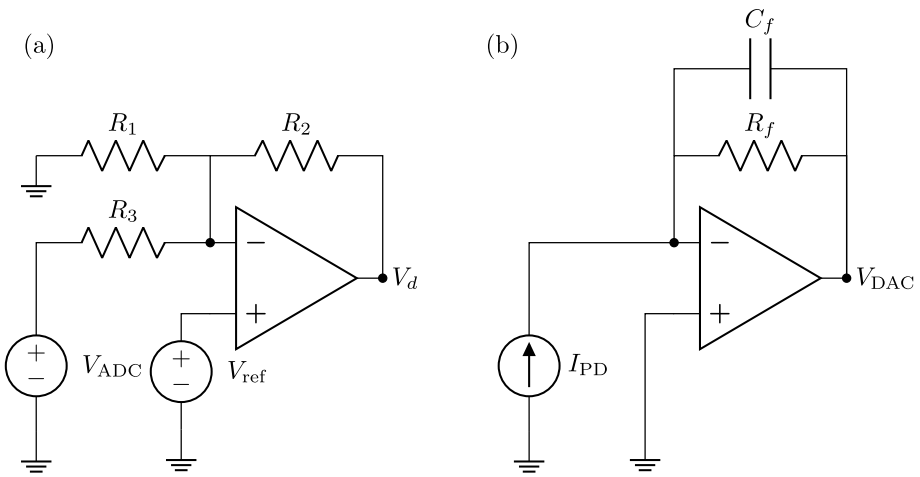

Fig. 24 FPGA: Op-amp gain stage (left) and TIA circuit (right)

Lumerical, sampled at 1001 equidistant frequency samples over the range [176.3, 214.1] THz. A wideband CVF macromodel with 40 poles is subsequently derived, achieving an accuracy, defined as the maximum error between the data and the model, of -50 dB. Half of the samples are used for training, whereas the remaining half are used for validation. The baseband frequency shift is set to $f_c = 193.41$ THz, corresponding to the center of the optical frequency range. A standard bottom-up approach is used to select the required number of poles [32]. Finally, a wavelength-tunable equivalent circuit is derived from the state-space representation.

Because the coupler's group delay must be approximated by a finite number of poles and due to its wavelength-dependent behavior, the wideband CVF macromodel needs a large number of poles, resulting in a SPICE model with many controlled sources. Given that the programmable mesh consists of 16 such models, this may significantly slow down simulation times. To this end, a second narrowband SPICE model is computed for comparison, now covering the narrowband frequency range [192.9, 193.9] THz, maintaining a high accuracy of -60 dB but using only 3 poles. As will be shown, the resulting equivalent circuit substantially speeds up simulation times; however, its validity is limited to a narrower bandwidth.

In [34], a compact, low-power phase shifter based on photonic microelectromechanical system (MEMS) actuation is demonstrated on IMEC's iSiPP50G silicon photonics foundry platform. In this numerical example, the device is adopted as the phase-shifting element within the analog gates of the photonic FPGA. An ideal SPICE model, assuming linear operation, is derived from the extracted device characteristics reported in [34]. The model is expressed as

$$\begin{aligned} A_o(t) &= IL \cdot A_i(t - \Delta t) \\ \phi_o(t) &= \phi_i(t - \Delta t) + \frac{2\pi n_{eff} f_c}{c} L + 2\pi \frac{V_d - v_0}{v_1 - v_0} \end{aligned} \tag{22}$$

For the silicon waveguide, the effective index (n_{eff}) and group index (n_g) are taken as $n_{eff} = 2.4$ and $n_g = 4.0$. Assuming a total phase shifter length of $L = 100$ μm, with 50 μm of active waveguide region, the group delay is calculated as $\Delta t = \frac{n_g L}{c} = 1.4$ ps. Based on the simulated phase response in [34], the linear operating region of the device is set by $v_0 = 6$ V and $v_1 = 32$ V. The insertion loss (IL) is modeled as 0.24 dB, representing an intermediate value between the reported minimum and maximum IL values of 0.16 dB and 0.32 dB, respectively. The response time of the device is modeled using an RC filter and is set according to the 3 dB bandwidth reported in [34].

The control electronics for the MEMS phase shifter consist of an ideal voltage source, representing the output of the analog-to-digital converter (ADC), followed by a voltage gain stage to provide the required drive voltage. The gain stage scales the ADC's 3.3V voltage swing to a level compatible with the drive voltage requirements of the phase shifter. On the receiver side, a TIA is adopted to convert the photocurrent generated by the photodetector into a voltage signal compatible with the digital-to-analog converter (DAC) input. A schematic diagram of both control and receiver electronics is illustrated in Fig. 24. Both the gain stage and TIA are modeled using ideal op-amps in LTspice and are assumed to operate within their linear regions. Under these linear operating conditions, the overall system is modeled according to the SSR scheme.

The resulting programmable mesh comprises 16 2×2 splitters, 16 phase shifters, 16 gain stages and 16 TIA circuits. Once the equivalent circuit of the photonic FPGA

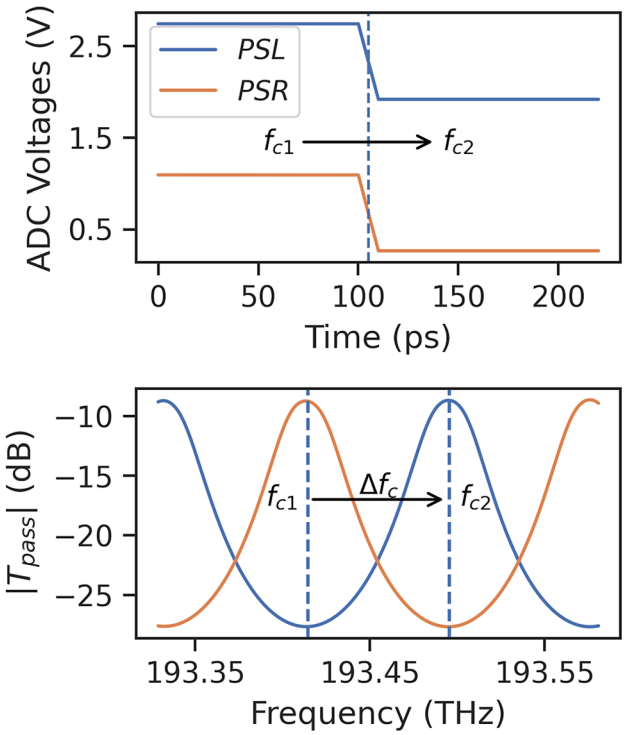

Fig. 25 FPGA: Active tuning of the double-ring filter. PSR and PSL denote the phase shifter control voltages applied to the analog gates within the right and left arms of the rings, respectively

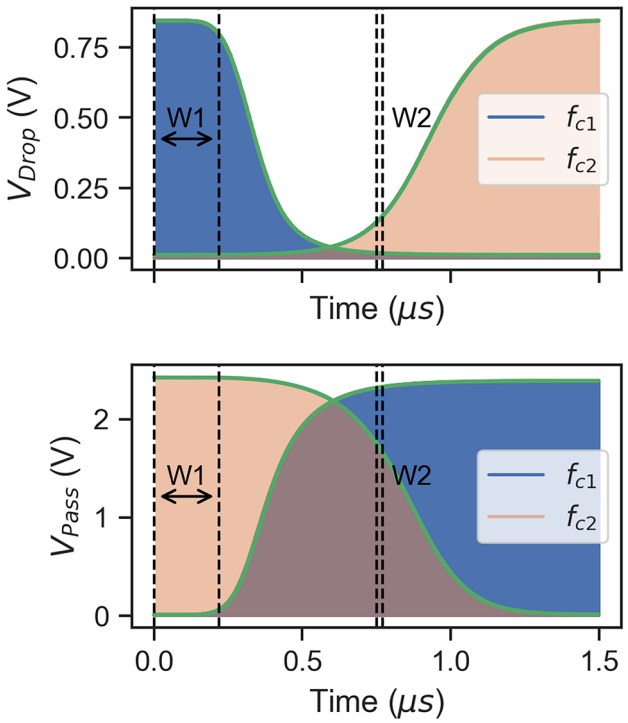

Fig. 26 FPGA: Transient simulation illustrating the switching behavior of the programmable circuit. The blue and orange surfaces represent OOK signals modulated onto carrier frequencies f_{c_1} and f_{c_2}, respectively, as obtained from SPICE simulations. The green envelope corresponds to the output of the compact time-varying instantaneous model. W1 and W2 denote the time-windows used for the plots in Fig. 25 and Fig. 27, respectively

is constructed in SPICE by interconnecting all relevant electronic, optoelectronic, and photonic building blocks, a transient analysis is performed to assess the active tuning behavior and switching functionality of the system. Two OOK signals, u_1 and u_2, each encoding a different bit sequence at a datarate of 500Mbs, are injected at the inputs of the combiner. These signal are modulated onto optical carrier frequencies $f_{c1} = 193.41$ THz and $f_{c2} = f_{c1} + FSR/2$, where FSR denotes the free spectral range of the double-ring resonator filter. Initially, the analog gates within the rings (green couplers in Fig. 22) are configured to align the filter's passband with f_{c1}, thus routing u_1 to the pass port while directing u_2 to the drop port. Subsequently, the control voltages applied to the phase shifters are adjusted to shift the filter's passband to f_{c2}, thereby reversing the routing configuration: signal u_2 is now directed to the pass port, while u_1 is routed to the drop port. The ADC output voltages, driving the phase shifters via the gain stage, and their effect on the filter response are illustrated in Fig. 25.

To validate the SPICE output response, the analog front-end and phase shifters are simulated independently within the SPICE environment. The resulting output waveforms are exported and applied as input excitations to a time-varying instantaneous model that captures the envelope of the OOK output signals. This model is defined as:

$$P_{i,l} = A_i^2 G_{\text{TIA}} |T_l(f_{c_i}, \mathbf{V}_d(t))|^2 \tag{23}$$

where f_{c_i} denotes the optical carrier frequency of the i^{th} input signal, A_i is the corresponding amplitude, and G_{TIA} is the transimpedance of the TIA stage. T_l represents the power transmission from input to output port, computed using a digital clone of the photonic FPGA in Luceda Photonics [33]. The vector $\mathbf{V}_d(t)$, obtained from a transient SPICE

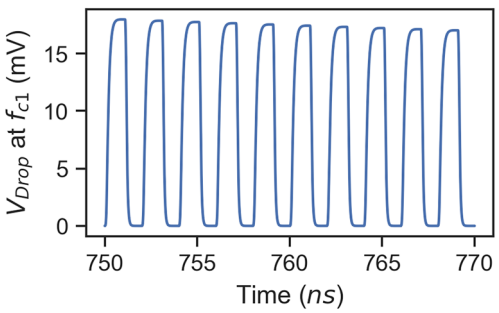

Fig. 27 FPGA: Zoom-in of the transient simulation in Fig. 26 showing the OOK signal modulated onto carrier frequency f_{c1} at the drop port of the double-ring resonator structure

simulation, contains the voltages applied to the input ports of the various phase shifters. While this model does not account for the dynamic and transient effects associated with the wavelength dispersion of the double-ring filter, it can be used to simulate the switching behavior of the circuit.

Fig. 26 presents the simulated outputs at the drop and pass ports of the double-ring resonator filter, while Fig. 27 zooms in at the drop port response over a smaller time window. The output of the instantaneous model closely matches the envelope of the OOK signals obtained from the SPICE simulation, verifying the correctness of the simulated switching behavior. The slowly varying envelope modulated onto the OOK signals reflects the response time of the phase shifters and determines the switching dynamics required to reroute the modulated carriers between the drop and pass ports. The CPU time for the compact equivalent narrowband model was 832.8 s, whereas the wideband model required 13342.8 s. Although the wideband model supports simulation across a broader wavelength range, this increased flexibility comes at the cost of higher computational complexity-highlighting the trade-off between model generality and simulation efficiency.

Although the compact equivalent narrowband circuit utilizes only three poles, the CPU time required for transient simulation remains relatively high compared to the preceding two numerical examples. This increased computational cost is primarily attributed to the substantial disparity in time scales between the slowly varying control signals and the high-speed RF modulation. Resolving the rapid transitions of the OOK bit sequence necessitates the use of small time steps over an extended simulation window, thereby increasing the computational burden. To address this limitation, future work will explore more advanced co-simulation strategies aimed at enhancing simulation efficiency.

8 Conclusion

This study presents SPICE-compatible, wavelength-tunable equivalent circuits that enable intricate co-simulation of photonic–electronic systems across multiple wavelengths. These circuits are derived from baseband state-space and pole-residue representations using synthesis techniques adapted from electronic system design. Furthermore, a novel interface circuit is proposed to enable seamless integration of third-party active and passive SPICE models described using the scattering wave formalism. By incorporating active device models that accurately represent electrical input and output impedances, the framework enables effective co-simulation with control and receiver electronics. Three relevant application examples are discussed, highlighting the effectiveness of the proposed framework in capturing the intricate dynamics and dispersive nature of photonic-electric chips.

Author Contributions All authors contributed to the study conception and design. Material preparation, data collection, and analysis were performed by Thijs Ullrick. The first draft of the manuscript was written by Thijs Ullrick, and all authors commented on previous versions of the manuscript. All authors read and approved the final manuscript.

Funding This work is supported by the Flemish Research Foundation (FWO-Vlaanderen G031421N), the Flanders AI Research Program, the Strategic Research Program of the VUB (SRP-78), and the Research Council of the VUB.

Data Availability No datasets were generated or analyzed during the current study.

Declarations

Conflict of interest The authors declare no Conflict of interest.

References

1. Harris, N.C., Carolan, J., Bunandar, D., Prabhu, M., Hochberg, M., Baehr-Jones, T., Fanto, M.L., Smith, A.M., Tison, C.C., Alsing, P.M., Englund, D.: Linear programmable nanophotonic processors. Optica **5**(12), 1623–1631 (2018). https://doi.org/10.1364/OPTICA.5.001623
2. Andersen, U.L.: Photonic chip brings optical quantum computers a step closer. Nature **591**(7848), 40–41 (2021). https://doi.org/10.1038/d41586-021-00488-z
3. ...Arrazola, J.M., Bergholm, V., Brádler, K., Bromley, T.R., Collins, M.J., Dhand, I., Fumagalli, A., Gerrits, T., Goussev, A., Helt, L.G., Hundal, J., Isacsson, T., Israel, R.B., Izaac, J., Jahangiri, S., Janik, R., Killoran, N., Kumar, S.P., Lavoie, J., Lita, A.E., Mahler, D.H., Menotti, M., Morrison, B., Nam, S.W., Neuhaus, L., Qi, H.Y., Quesada, N., Repingon, A., Sabapathy, K.K., Schuld, M., Su, D., Swinarton, J., Száva, A., Tan, K., Tan, P., Vaidya, V.D., Vernon, Z., Zabaneh, Z., Zhang, Y.: Quantum circuits with many photons on a programmable nanophotonic chip. Nature **591**(7848), 54–60 (2021). https://doi.org/10.1038/s41586-021-03202-1
4. Hsu, C.-P., Li, B., Solano-Rivas, B., Gohil, A.R., Chan, P.H., Moore, A.D., Donzella, V.: A review and perspective on optical phased array for automotive LiDAR. IEEE J. Sel. Top. Quantum Electron. **27**(1), 1–16 (2021). https://doi.org/10.1109/JSTQE.2020.3022948
5. Mena, P.V., Morikuni, J.J., Kang, S.-M., Harton, A.V., Wyatt, K.W.: A comprehensive circuit-level model of vertical-cavity surface-emitting lasers. J. Lightw. Technol. **17**(12), 2612–2632 (1999). https://doi.org/10.1109/50.809684
6. Zhang, Z., Wu, R., Wang, Y., Zhang, C., Stanton, E.J., Schow, C.L., Cheng, K.-T., Bowers, J.E.: Compact modeling for silicon photonic heterogeneously integrated circuits. J. Lightw. Technol. **35**(14), 2973–2980 (2017). https://doi.org/10.1109/JLT.2017.2706721
7. Tanaka, S., Usuki, T., Tanaka, Y.: Accurate SPICE model of forward-biased silicon PIN Mach–Zehnder modulator for an energy-efficient multilevel transmitter. J. Lightwave Technol. **36**(10), 1959–1969 (2018). https://doi.org/10.1109/JLT.2018.2797184
8. Kim, M., Jo, Y., Lischke, S., Mai, C., Zimmermann, L., Choi, W.-Y.: A temperature-aware large-signal SPICE model for depletion-type silicon ring modulators. IEEE Photon. Technol. Lett. **33**(17), 947–950 (2021). https://doi.org/10.1109/LPT.2021.3098760
9. Shin, M., Ban, Y., Yu, B.-M., Kim, M.-H., Rhim, J., Zimmermann, L., Choi, W.-Y.: A linear equivalent circuit model for depletion-type silicon microring modulators. IEEE Trans. Electron Devices **64**(3), 1140–1145 (2017). https://doi.org/10.1109/TED.2017.2648861

10. Jalali, M., Moravvej-Farshi, M.K., Masudy-Panah, S., Nabavi, A.: An equivalent lumped circuit model for thin avalanche photodiodes with nonuniform electric field profile. J. Lightwave Technol. **28**(23), 3395–3402 (2010)
11. Dai, D., Piels, M., Bowers, J.E.: Monolithic germanium/silicon photodetectors with decoupled structures: resonant APDs and UTC photodiodes. IEEE J. Sel. Top. Quantum Electron. **20**(6), 43–56 (2014). https://doi.org/10.1109/JSTQE.2014.2322443
12. Piels, M., Ramaswamy, A., Bowers, J.E.: Nonlinear modeling of waveguide photodetectors. Opt. Express. **21**(13), 15634–15644 (2013). https://doi.org/10.1364/OE.21.015634
13. Wang, B., Li, C., Chen, C.-H., Yu, K., Fiorentino, M., Beausoleil, R.G., Palermo, S.: A compact Verilog-a model of silicon carrier-injection ring modulators for optical interconnect transceiver circuit design. J. Lightwave Technol. **34**(12), 2996–3005 (2016). https://doi.org/10.1109/JLT.2015.2505239
14. Sorace-Agaskar, C., Leu, J., Watts, M.R., Stojanovic, V.: Electro-optical co-simulation for integrated CMOS photonic circuits with VerilogA. Opt. Express. **23**(21), 27180–27203 (2015). https://doi.org/10.1364/OE.23.027180
15. Shawon, M.J., Saxena, V.: Rapid simulation of photonic integrated circuits using Verilog-A compact models. IEEE Trans. Circuits Syst. I: Regular Papers **67**(10), 3331–3341 (2020). https://doi.org/10.1109/TCSI.2020.2983303
16. Gunupudi, P., Smy, T., Klein, J., Jakubczyk, Z.J.: Self-Consistent simulation of opto-electronic circuits using a modified nodal analysis formulation. IEEE Trans. Adv. Packag. **33**(4), 979–993 (2010). https://doi.org/10.1109/TADVP.2010.2054089
17. Foucauld, E., Rozeau, O., Myko, A., Fowler, D., Virot, L., Gays, F.: Compact modeling of photonic devices in Verilog-A for integrated circuit design. Solid-State Electron. **200**, 108538 (2023). https://doi.org/10.1016/j.sse.2022.108538
18. Ming, D., Wang, Y., Wang, Z., Wang, K.X., Qiu, C., Tan, M.: EPHIC models: general SPICE photonic models for closed-loop electronic-photonic co-simulation. IEEE Trans. Circuits Syst. I: Regular Papers **71**(4), 1819–1831 (2024). https://doi.org/10.1109/TCSI.2024.3353459
19. Zhang, S., Fan, X., Chen, N., Qiu, C., Wang, X., Wang, K.X., Xu, J., Tan, M.: Compact photonic model based on coupled-mode theory for nonlinear interactions in electronic-photonic co-simulation. Opt. Express **32**(16), 27599–27613 (2024). https://doi.org/10.1364/OE.529044
20. Zhang, S., Fan, X., Chen, N., Wang, K.X., Xu, J., Tan, M.: A Verilog-A compact model for four-wave mixing supporting electronic-photonic co-simulation. In: 2024 2nd International Symposium of Electronics Design Automation (ISEDA), pp. 16–19 (2024). https://doi.org/10.1109/ISEDA62518.2024.10617775
21. Ye, Y., Spina, D., Deschrijver, D., Bogaerts, W., Dhaene, T.: Time-domain compact macromodeling of linear photonic circuits via complex vector fitting. Photon. Res. **7**(7), 771 (2019). https://doi.org/10.1364/PRJ.7.000771
22. Spina, D., Ye, Y., Deschrijver, D., Bogaerts, W., Dhaene, T.: Complex vector fitting toolbox: a software package for the modelling and simulation of general linear and passive baseband systems. Electron. Lett. **57**(10), 404–406 (2021). https://doi.org/10.1049/ell2.12116
23. Ye, Y., Ullrick, T., Bogaerts, W., Dhaene, T., Spina, D.: SPICE-compatible equivalent circuit models for accurate time-domain simulations of passive photonic integrated circuits. J. Lightwave Technol. **40**(24), 7856–7868 (2022). https://doi.org/10.1109/JLT.2022.3206818
24. Ullrick, T., Spina, D., Bogaerts, W., Dhaene, T.: Wideband parametric baseband macromodeling of linear and passive photonic circuits via complex vector fitting. Sci. Rep. **13**(1), 15407 (2023). https://doi.org/10.1038/s41598-023-41227-w
25. Williams, D.: Traveling waves and power waves: building a solid foundation for microwave circuit theory. IEEE Microwave Mag. **14**(7), 38–45 (2013). https://doi.org/10.1109/MMM.2013.2279494
26. Yeom, K.-W.: Microwave Circuit Design: A Practical Approach Using ADS. Prentice Hall, New York (2015)
27. Chou, C.-C., Schutt-Ainé, J.E.: Equivalent circuit synthesis of multiport s parameters in pole-residue form. IEEE Trans. Compon. Packag. Manuf. Technol. **11**(11), 1971–1979 (2021). https://doi.org/10.1109/TCPMT.2021.3115113
28. Romano, D., Antonini, G., Grossner, U., Kovačević-Badstübner, I.: Circuit synthesis techniques of rational models of electromagnetic systems: a tutorial paper. Int. J. Numer. Modell.: Electron. Netw. Devices Fields **32**(5), 2612 (2019). https://doi.org/10.1002/jnm.2612
29. Antonini, G.: SPICE equivalent circuits of frequency-domain responses. IEEE Trans. Electromagn. Compat. **45**(3), 502–512 (2003). https://doi.org/10.1109/TEMC.2003.815528. (**Conference Name: IEEE Transactions on Electromagnetic Compatibility**)
30. Jeruchim, M.C., Balaban, P., Shanmugan, K.S., Jeruchim, M.C. (eds.): Simulation of Communication Systems: Modeling, Methodology, and Techniques, 2nd ed edn. Information technology-transmission, processing, and storage. Kluwer Academic/Plenum Publishers, New York (2000)
31. Neumayer, R., Haslinger, F., Stelzer, A., Weigel, R.: Synthesis of SPICE-compatible broadband electrical models from n-port scattering parameter data. In: IEEE International Symposium on Electromagnetic Compatibility, vol. 1, pp. 469–474. IEEE, Minneapolis, MN, USA (2002). https://doi.org/10.1109/ISEMC.2002.1032524
32. Stevens, N., Deschrijver, D., Dhaene, T.: Fast automatic order estimation of rational macromodels for signal integrity analysis. In: 2007 IEEE Workshop on Signal Propagation on Interconnects, pp. 89–92. IEEE, Ruta di Camogli, Italy (2007). https://doi.org/10.1109/SPI.2007.4512218
33. Luceda Photonics [Online]. Available: https://www.lucedaphotonics.com. Accessed: 2025
34. Edinger, P., Takabayashi, A.Y., Errando-Herranz, C., Khan, U., Sattari, H., Verheyen, P., Bogaerts, W., Quack, N., Gylfason, K.B.: Silicon photonic microelectromechanical phase shifters for scalable programmable photonics. Opt. Lett. **46**(22), 5671–5674 (2021). https://doi.org/10.1364/OL.436288